Magnetic Moment Fragmentation in an All-in–All-out Pyrochlore $Nd_2Sn_2O_7$

Yi Luo,[1,*] Matthew Powell,[2] Joseph A. M. Paddison,[1] Brenden R. Ortiz,[3]
J. Ross Stewart,[4] Joseph W. Kolis,[2] and Adam A. Aczel[1,†]

[1] *Neutron Scattering Division, Oak Ridge National Laboratory, Oak Ridge, Tennessee 37831, USA*
[2] *Department of Chemistry, Clemson University, Clemson, South Carolina 29634-0973, USA*
[3] *Materials Science and Technology Division, Oak Ridge National Laboratory, Oak Ridge, Tennessee 37831, USA*
[4] *ISIS Neutron and Muon Source, Rutherford Appleton Laboratory, Didcot OX11 0QX, UK*

We report single-crystal neutron spectroscopy and bulk characterization on hydrothermally grown $Nd_2Sn_2O_7$, revealing magnetic moment fragmentation embedded within the all-in–all-out ordered state. The spectra show a nearly flat band with pinch-point-like momentum dependence, accompanied by dispersive branches that generate half-moon features across multiple Brillouin zones. These defining signatures are captured quantitatively by a minimal dipolar–octupolar spin Hamiltonian, demonstrating excellent agreement between experiment and theory. The higher flat-mode energy helps account for the absence of dynamical interference in prior μSR studies, while the lack of any photon-like excitation imposes strict constraints on the proposed Coulombic antiferromagnet scenario. Our results extend moment fragmentation to $Nd_2Sn_2O_7$ and identify it as a clean, tractable platform for quantitative exploration of emergent gauge-field physics and multipolar spin-wave dynamics in frustrated magnets.

Introduction–Geometrical frustration on the pyrochlore lattice of corner-sharing tetrahedra gives rise to spin-ice (Coulombic) physics [1–4]. In classical spin ice, strong local $\langle 111\rangle$ Ising anisotropy together with effective ferromagnetic nearest-neighbor exchange enforces the "two-in, two-out" rule on each tetrahedron [5, 6], producing an extensively degenerate manifold with Pauling entropy [7] and dipolar correlations that yield pinch-point patterns in diffuse scattering [8]. These results motivate the quantum spin-ice (QSI) scenario [9], in which anisotropic exchanges induce tunneling between ice configurations and stabilize a $U(1)$ quantum spin liquid (QSL) with an emergent gauge field and gapless photon-like excitations.

Amid the intense search for materials that realize QSI physics, the dipolar–octupolar (DO) rare-earth pyrochlores $R_2M_2O_7$ (R = Ce, Nd, Sm; M = Zr, Hf, Sn, Ti, Pb) [10–42] have emerged as a particularly compelling family. Because the ground-state doublet of DO pyrochlores is typically well separated from the first crystal-electric-field (CEF) excitation by $\Delta_{\mathrm{CEF}} \gtrsim 100\,\mathrm{K}$, while the nearest-neighbor interactions are only $J \sim 1\,\mathrm{K}$, the low-energy physics is well captured by an effective pseudospin-$\frac{1}{2}$ description in terms of operators $\tau_i^{x,y,z}$ [43]. In the local frame with $\hat{\mathbf{z}} \parallel \langle 111\rangle$ and $\hat{\mathbf{y}}$ along a twofold rotation axis, only τ_i^z has a nonzero magnetic-dipole matrix element, whereas τ_i^x and τ_i^y have leading octupolar character. From a symmetry standpoint, τ_i^x and τ_i^z transform as components of a dipolar vector under time reversal and D_{3d} symmetry, while τ_i^y transforms as a component of the magnetic octupole tensor [43, 44]. Within the DO manifold, the symmetry-allowed nearest-neighbor exchange reduces, after an appropriate pseudospin rotation, to the compact "XYZ" Hamiltonian [25, 43]:

$$\mathcal{H}_{\mathrm{XYZ}}^{\mathrm{DO}} = \sum_{\langle ij\rangle} \Big(\tilde{J}_x\, \tilde{\tau}_i^{\tilde{x}} \tilde{\tau}_j^{\tilde{x}} + \tilde{J}_y\, \tilde{\tau}_i^{\tilde{y}} \tilde{\tau}_j^{\tilde{y}} + \tilde{J}_z\, \tilde{\tau}_i^{\tilde{z}} \tilde{\tau}_j^{\tilde{z}} \Big). \quad (1)$$

Here, the pseudospin-$\frac{1}{2}$ operators $\tilde{\tau}_i^{\tilde{x},\tilde{y},\tilde{z}}$ are defined in a rotated local frame $(\tilde{x}, \tilde{y}, \tilde{z})$ obtained by a rotation by a material-dependent angle ϑ about the local y axis; consequently $\tilde{\tau}_i^{\tilde{y}} = \tau_i^y$ retains its octupolar character, whereas $\tilde{\tau}_i^{\tilde{x}}$ and $\tilde{\tau}_i^{\tilde{z}}$ are linear combinations of τ_i^x and τ_i^z that transform as magnetic dipole components. Theoretical studies [45–48] show that DO pyrochlores can host a variety of symmetry-enriched $U(1)$ QSL phases; possible realizations have recently been reported in Ce-based pyrochlores [10–20].

By contrast, Nd-based pyrochlores occupy a different region of the DO phase diagram and stabilize the all-in–all-out (AIAO) antiferromagnetic state, in which the four moments on each tetrahedron point either all toward or all away from the center, alternating on neighboring tetrahedra [Fig. 1(i)]. Yet this order is far from trivial: geometric frustration together with the peculiar symmetry of the DO doublet enables *moment fragmentation* [25, 49, 50], wherein a single microscopic moment decomposes into divergence-full and divergence-free components. We note that the mechanism relevant to Nd-based pyrochlores [25, 50] arises from multipolar couplings and therefore differs from the proposal of Ref. [49]. A prototypical case is $Nd_2Zr_2O_7$ [21–31], in which neutron diffraction and spectroscopy reveal antiferromagnetic Bragg peaks coexisting with a gapped and flat band at $\sim$70 μeV whose structure factor displays the characteristic pinch-point pattern [23]. Theory [25, 28] traces these phenomena to the XYZ model [Eq. (1)]: a ferromagnetic $\tilde{J}_{\tilde{z}} < 0$ in the local frame selects AIAO order of the $\tilde{\tau}^{\tilde{z}}$ component, while an antiferromagnetic $\tilde{J}_{\tilde{x}} > 0$ frustrates the transverse $\tilde{\tau}^{\tilde{x}}$ fluctuations. For $\tilde{J}_{\tilde{x}} < 3|\tilde{J}_{\tilde{z}}|$, the ground state hosts long-range AIAO order, and the total moment naturally fragments into static and fluctuating parts,

$$\mathbf{m}_i = g_z\, \mu_{\mathrm{B}} \big[\cos\vartheta\, \tilde{\tau}_i^{\tilde{z}} + \sin\vartheta\, \tilde{\tau}_i^{\tilde{x}} \big]\, \hat{z}_i, \quad (2)$$

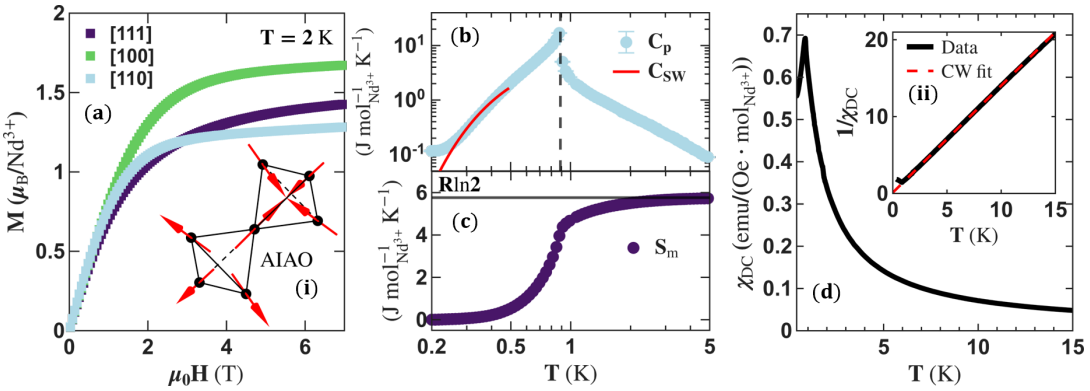

FIG. 1. (a) Magnetization $M(H)$ at $T = 2$ K for $Nd_2Sn_2O_7$ measured along [100], [111], and [110]. Inset (i): schematic of the all-in–all-out (AIAO) order below T_N. (b) Heat capacity $C_p(T)$ after subtracting the $La_2Sn_2O_7$ lattice contribution; the vertical dashed line marks $T_N = 0.89(3)$ K; the red curve marks the calculated spin-wave contribution $C_{SW}(T)$. (c) Magnetic entropy $S_{mag}(T) = \int_0^T (C_p/T')\,dT'$ recovering $R\ln 2$ by ∼5 K. (d) DC susceptibility $\chi(T)$ of pulverized single crystals showing a peak at T_N. Inset (ii): Curie–Weiss fit to $\chi^{-1}(T)$ over 2–10 K, yielding $\theta_{CW} = -0.08(1)$ K and $\mu_{eff} = 2.397(2)\,\mu_B/Nd^{3+}$.

where g_z is the longitudinal g factor and $\hat{z}_i$ the local easy axis at site i. The $\tilde{\tau}_i^{\tilde{z}}$ piece forms the static ordered moment $m_{ord} = 1.26(2)$ μ_B/Nd^{3+} [21], whereas $\tilde{\tau}_i^{\tilde{x}}$ remains dynamic, generating the flat band with spin-ice–like correlations. Upon warming just above the Néel temperature $T_N \approx 0.4$ K, this band softens to the elastic line, realizing a gapless Coulomb phase and signaling the proximity of $Nd_2Zr_2O_7$ to the U(1) QSL regime [29, 30].

Establishment of moment fragmentation in $Nd_2Zr_2O_7$ prompts the question of its prevalence across the Nd pyrochlore family. Neutron spectroscopy on $Nd_2Hf_2O_7$ [32–34] and Nd_2ScNbO_7 [51, 52] confirms AIAO order together with dynamical spin-ice-like correlations, the hallmarks of fragmentation. In contrast, the divergence free component, and thus fragmentation, has been argued to be absent in $Nd_2Sn_2O_7$ [35], which enters an AIAO phase below $T_N \approx 0.91$ K with a comparatively large ordered moment $m_{ord} = 1.708(3)\,\mu_B/Nd^{3+}$ (see Table I). The central experimental claim is the observation of spontaneous muon spin precession in zero field μSR below T_N, absent in analogous measurements on $Nd_2Zr_2O_7$ [24] and $Nd_2Hf_2O_7$ [33]; this has been taken to indicate that no dynamic internal fields exist on the μSR timescale to obscure the static order in $Nd_2Sn_2O_7$. Taken together with the observation that $C_p \propto T^3$ below T_N, these results motivated the proposal that $Nd_2Sn_2O_7$ realizes a Coulombic antiferromagnet (CAF), stabilized by further neighbor interactions and characterized by long range spin ice entanglement [53]. The CAF phase is predicted to exhibit distinctive spectroscopic signatures, including gapped monopole continuums and gapless, linearly dispersing photon-like excitations. Following Ref. [35], work on Nd_2GaSbO_7 [54] likewise finds no conclusive evidence of fragmentation within the AIAO state; instead a gapped magnetic mode appears at $\hbar\omega \approx 0.25$ meV without the Q-dependence characteristic of spin-ice correlations.

Despite suggestive bulk characterizations and μSR results on $Nd_2Sn_2O_7$ [35, 55], these probes cannot discriminate a fragmented AIAO state from a conventional AIAO phase, nor can they establish the proposed CAF. A decisive test requires single-crystal neutron scattering, which directly measures the dynamical structure factor and can reveal either the pinch-point flat band characteristic of moment fragmentation or the photon/monopole signatures expected for a CAF. Such studies were long impeded by the difficulty of growing sizable single crystal $Nd_2Sn_2O_7$, a challenge recently overcome by advances in the hydrothermal growth method [56]. To address whether fragmentation is ubiquitous in Nd pyrochlores, we report the first bulk characterization and neutron spectroscopy results on single crystal $Nd_2Sn_2O_7$. These measurements uncover the aforementioned spectroscopic signatures of moment fragmentation in $Nd_2Sn_2O_7$ and delineate its low temperature magnetic properties, thereby resolving the controversy and clarifying the scope of fragmentation across Nd pyrochlores.

Results– Single crystal $Nd_2Sn_2O_7$ samples were prepared *via* a hydrothermal method. Magnetization $M(H)$ was measured along [100], [111], and [110] directions [Fig. 1(a)]. The saturation moments are ordered as $m^{sat}_{100} > m^{sat}_{111} > m^{sat}_{110}$, consistent with expectations for a magnetic pyrochlore with easy axis anisotropy [57]. Heat capacity after subtracting the lattice contribution [Fig. 1(b)], shows a λ type peak at $T_N = 0.89(3)$ K. The integrated magnetic entropy $S_{mag}(T)$ approaches the full $R\ln 2$ of the ground state doublet by ∼ 5 K [Fig. 1(c)]. The dc susceptibility of pulverized single crystals of $Nd_2Sn_2O_7$ exhibits a clear anomaly at T_N [Fig. 1(d)]; a Curie Weiss fit over 2–10 K yields $\theta_{CW} = -0.08(1)$ K and an effective moment $\mu_{eff} =$

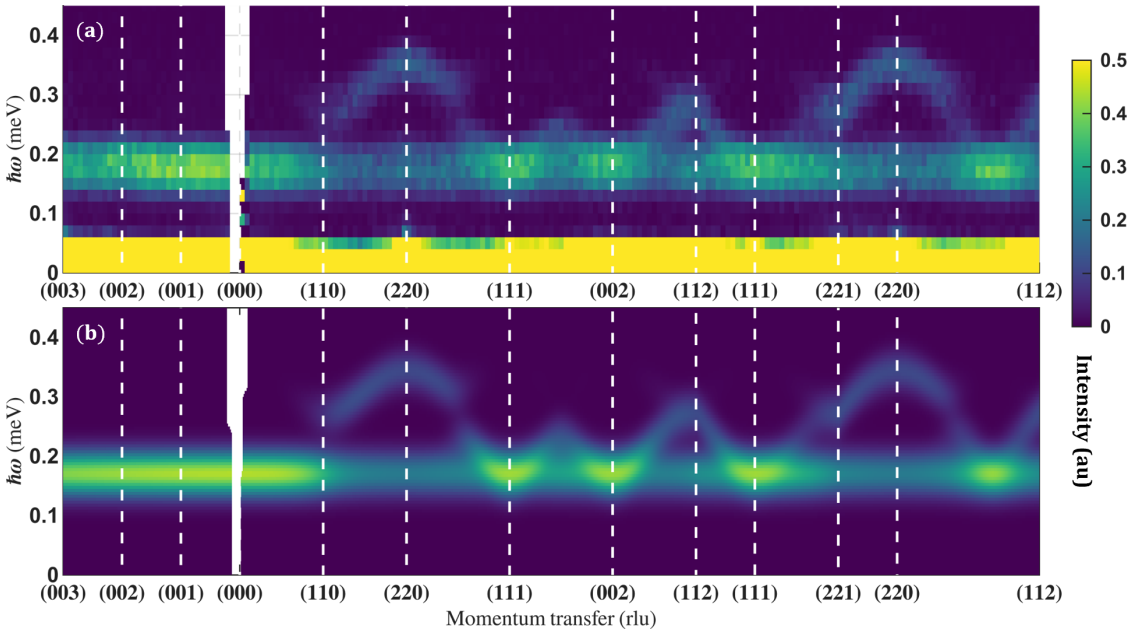

FIG. 2. (a) False color map of inelastic scattering intensity $S(\mathbf{Q},\omega)$ versus energy transfer $\hbar\omega$ and momentum transfer Q along a path connecting the labeled high symmetry points. Data were taken at $T = 0.25$ K with incident energy $E_i = 2.19$ meV on the LET spectrometer (elastic resolution FWHM ≈ 0.07 meV), integrated over a perpendicular momentum window of ± 0.1 Å^{-1}, and not symmetrized. (b) Simulated intensity from the spin-wave model of Ref. [25] with parameters $(\tilde{J}_x, \tilde{J}_y, \tilde{J}_z) = (0.10(2), 0.00(1), -0.075(2))$ meV, convolved with the LET energy resolution and scaled by a single global factor to match the data.

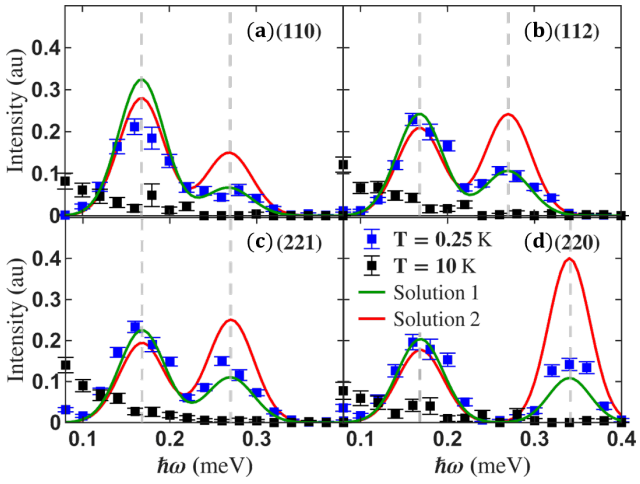

FIG. 3. (a–d) Constant-Q energy cuts at the indicated points, integrated over ± 0.1 rlu along each principal direction and measured with $E_i = 2.19$ meV. Blue/black: $T = 0.25$ K/10 K. Green/red: simulations for Solution 1/Solution 2, averaged over the same Q-windows as the data, convolved with the LET energy resolution, and scaled by a single global factor (per solution) to match the total intensity across panels. Experimental spectra are averaged over symmetry-equivalent points in the (HHL) plane using space group $Fd\bar{3}m$. Gray dashed lines mark the calculated spin-wave energies.

2.397(2) μ_B/Nd^{3+} [Fig. 1(ii)]. For inelastic neutron spectroscopy, we measured a co-aligned, coarse-grained assembly on the LET cold-neutron chopper spectrometer at the ISIS Neutron and Muon Source (Rutherford Appleton Laboratory, UK). Details of the experimental methods are provided in the Supplemental Material.

An overview of the inelastic magnetic response of $Nd_2Sn_2O_7$ at $T = 0.25$ K, deep in the AIAO phase below T_N, is shown in Fig. 2(a). Magnetic Bragg peaks at (220) and (113) appear on the elastic line (see Fig. S2 of the Supplemental Material), reflecting the AIAO order of the divergence-full $\tilde{\tau}^{\tilde{z}}$ component [25], while the inelastic channel displays gapped spin-wave excitations. The spectrum comprises a nearly flat band and dispersive branches, with momentum and energy dependences closely resembling those in $Nd_2Zr_2O_7$ [23, 28] and $Nd_2Hf_2O_7$ [34]. Within the fragmentation framework [25], the nearly flat band corresponds to the divergence-free sector, while the dispersive branches reflect the divergence-full sector of the fluctuating $\tilde{\tau}^{\tilde{x}}$ component. Neither a monopole continuum nor a photon-like mode is observed in the accessible energy range $\hbar\omega \gtrsim 0.09$ meV.

To model the spectra we employ the spin-wave framework of Ref. [25]. The exchange set $(\tilde{J}_x, \tilde{J}_y, \tilde{J}_z)$ is obtained by fitting the calculated energies to the measured gaps of the flat band, $\Delta_1 = 0.168(2)$ meV, the dispersive branches at the zone boundary (100), $\Delta_2 = 0.270(4)$ meV, and the highest energy at the zone center (000), $\Delta_3 = 0.341(5)$ meV. This proce-

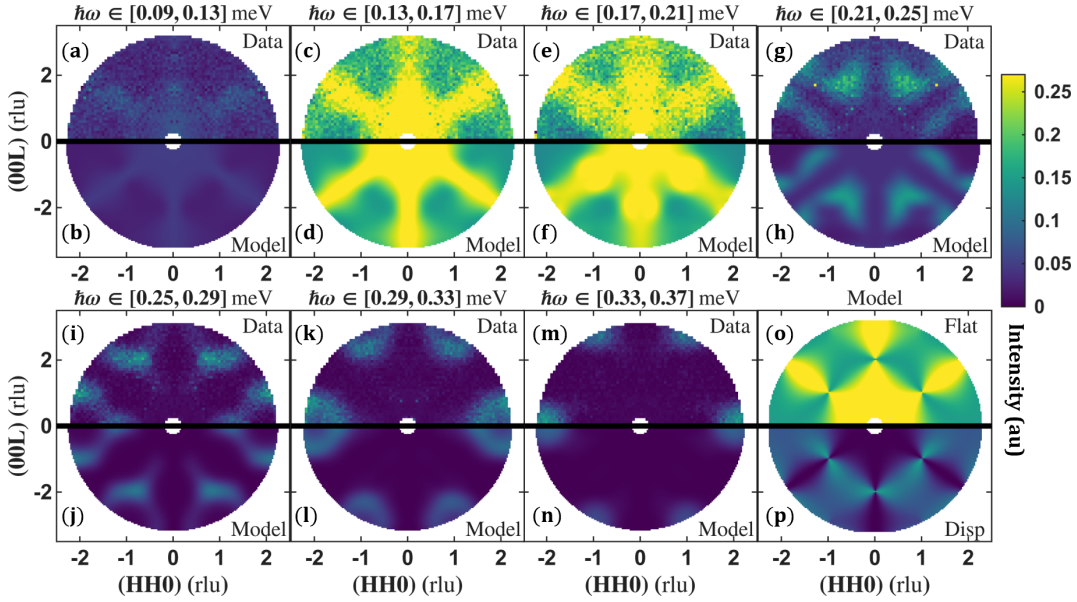

FIG. 4. (a,c,e,g,i,k,m) Constant energy Q maps collected at $T = 0.25$ K with $E_i = 2.19$ meV in the (HHL) plane. Data are integrated along $[K\bar{K}0]$ with $K \in [-0.07, 0.07]$ rlu, symmetrized in the (HHL) plane using space group $Fd\bar{3}m$. (b,d,f,h,j,l,n) Simulated Q maps from the spin wave model of Ref. [25] with parameters $(\tilde{J}_x, \tilde{J}_y, \tilde{J}_z) = (0.10(2)), 0.00(1), -0.075(2)))$ meV, convolved with the LET resolution and scaled by a single global factor to match the data. (o,p) Q-dependence of the simulated intensity for the flat band (o) and the dispersive branches (p).

dure yields two symmetry-related solutions: Solution 1, (0.10(2), 0.00(1), −0.075(2)) meV, and Solution 2, obtained by exchanging $\tilde{J}_x$ with $\tilde{J}_y$. Constant-Q energy cuts at representative high-symmetry points [Fig. 3], benchmarked against resolution-convolved simulations, show that only Solution 1 reproduces the relative spectral weights of the flat and dispersive modes. The simulated lineshapes match the experimental, resolution-limited linewidths, implying no detectable magnon damping. Simulated inelastic spectra based on Solution 1 are shown in Fig. 2(b), and constant-energy Q maps in Fig. 4. We find excellent agreement between the data and our simulations for both the dispersions and the structure factors across multiple Brillouin zones. The flat band at $\Delta_1 = 0.168(2)$ meV exhibits the characteristic pinch-point-like Q dependence [23, 25] [Figs. 4(a)–(d)], while the dispersive branches immediately above it display the characteristic 'half-moon' features [34, 58] [Figs. 4(e)–(h)]. The dispersive mode with higher energy reaches its band maximum at $\Delta_3 = 0.341(5)$ meV at the zone centers (220) and (113) [Figs. 4(i)–(n)].

With the exchange parameters determined, the rotation angle ϑ, which sets the relative degrees of the static and fluctuating moment components in Eq.2, can be estimated from $m_{\rm ord}/m_{\rm sat} = \cos\vartheta\langle\tilde{\tau}^{\tilde{z}}\rangle/S$, with $S = \frac{1}{2}$ [25, 28]. Using the reported ordered moment $m_{\rm ord} = 1.708(3)\,\mu_{\rm B}$ [35] and taking $m_{\rm sat} \approx \mu_{\rm eff} = 2.397(2)\,\mu_{\rm B}$ for an Ising-like ground state doublet [54], we obtain $\vartheta = 0.74(3)$ rad for $Nd_2Sn_2O_7$. The Curie Weiss temperature calculated from ϑ [25] is $\theta_{\rm CW}^{\rm cal} = 0.03(7)$ K,in reasonable agreement with our experimental fit. The calculated spin-wave contribution to the heat capacity, $C_{\rm SW}$, is shown in Fig. 1(b). The slight upturn of C_p below ∼0.25 K may stem from a nuclear contribution, similar to the behavior reported for $Nd_2Zr_2O_7$ [28]. Details of the spin-wave model and parameters determination are provided in the Supplemental Material.

Discussion– The bulk thermodynamic measurements on our hydrothermally grown single-crystal $Nd_2Sn_2O_7$, in particular the heat capacity C_p below $T_{\rm N}$ [Fig. 1(b)], are consistent with the powder results reported in Ref. [35]. However, the calculated spin-wave heat capacity $C_{\rm SW}$ accounts for most of the measured C_p in the range 0.2–0.5 K, a regime previously described by $C_p \propto T^3$ [35] and attributed to a linearly dispersing photon mode [35, 53].

Consistent with this picture, our neutron spectra es-

Sample	$m_{\rm ord}$ ($\mu_{\rm B}$)	$m_{\rm sat}$ ($\mu_{\rm B}$)	Δ_1 (meV)	ϑ (rad)
$Nd_2Zr_2O_7$	1.26(2)[21]	2.50*[28]	0.075(4)[28]	0.98(3)[28]
$Nd_2Hf_2O_7$	0.62(1)[32]	2.50[32]	0.094[34]	1.26[34]
Nd_2ScNbO_7	2.2(4)[51]	2.25(25)[51]	0.065(15)[51]	-
Nd_2GaSbO_7	1.59(5)[54]	2.37(1)[54]	0.253(6)[54]	-
$Nd_2Sn_2O_7$	1.708(3)[35]	2.397(2)*	0.168(2)	0.74(3)

TABLE I. Comparison of ordered moment $m_{\rm ord}$, saturation moment $m_{\rm sat}$, flat-mode gap Δ_1, and rotation angle ϑ for selected Nd pyrochlores. Entries for $m_{\rm sat}$ marked with an asterisk (*) are inferred from magnetic susceptibility rather than a CEF analysis.

tablish moment fragmentation in $Nd_2Sn_2O_7$ below T_N. Elastic Bragg peaks confirm AIAO order of the $\tilde{\tau}^{\tilde{z}}$ component, while the inelastic channel reveals gapped spin-wave excitations arising from the $\tilde{\tau}^{\tilde{x}}$ sector. The flat band at $\Delta_1 = 0.168(2)$ meV lies well above the dynamical window of zero-field μSR (estimated to be $\lesssim 0.05$ meV [35]), which likely accounts for the absence of μSR-detected dynamical interference with static order in $Nd_2Sn_2O_7$, in contrast to $Nd_2Zr_2O_7$ [24] and $Nd_2Hf_2O_7$ [33] where the substantially smaller Δ_1 renders such effects observable. Taken together, our neutron spectra rule out CAF excitations within the accessible energy range $\hbar\omega \gtrsim 0.09$ meV, while the prior μSR measurements likewise exclude low-energy modes with $\hbar\omega \lesssim 0.05$ meV. These combined constraints strongly limit the energy window available for CAF excitations and effectively rule out a dominant CAF phase in $Nd_2Sn_2O_7$.

Linear spin-wave calculations within the fragmentation framework [25] uniquely determine the exchange parameters $(\tilde{J}_x, \tilde{J}_y, \tilde{J}_z) = (0.10(2), 0.00(1), -0.075(2))$ meV. The near-vanishing $\tilde{J}_y$ disfavors any octupolar order of the τ^y component, in contrast to proposals for $Ce_2Sn_2O_7$ [16, 17] and $Ce_2Hf_2O_7$ [19]. The resulting simulations reproduce both the dispersions and the structure factors across multiple Brillouin zones with excellent fidelity. The calculated flat band displays the expected dynamical spin-ice correlations [Fig.4(o)] [25], while the broadened pinch-point pattern observed experimentally [Fig.4(a,c)] arises from finite energy resolution and contributions from the nearby dispersive mode [Fig.4(p)] close to the pinch-point positions. Higher-resolution probes (e.g. backscattering or neutron spin echo) will be essential to test whether a small CAF component coexists with the AIAO order and to search for a proximate ferromagnetic Coulomb phase just above T_N, motivated by the case of $Nd_2Zr_2O_7$ [29, 30].

Beyond the spin-ice context, our results place $Nd_2Sn_2O_7$ within a broader class of multipolar quantum magnets. Recent work on FeI_2 has shown that strong spin–orbit coupling can mix dipolar and quadrupolar channels, yielding collective modes that lie beyond conventional spin-wave theory [59]. Similarly, in UO_2, the coexistence of dipolar and quadrupolar order supports dispersive multipolar excitations that acquire neutron visibility through dipole–multipole mixing [60]. A similar mechanism operates in Nd-based dipole–octupole pyrochlores: in $Nd_2Sn_2O_7$, the octupolar component of the CEF doublet mixes with the dipolar sector, yielding AIAO order and gapped modes of mixed multipolar character. The resulting excitation spectrum cannot be understood within a purely dipolar picture, underscoring the broader significance of $Nd_2Sn_2O_7$ as a platform for probing multipolar quasiparticles in spin–orbit–entangled magnets.

Overall, our findings establish $Nd_2Sn_2O_7$ as a platform in which AIAO order supports magnetic moment fragmentation arising from well-characterized multipolar interactions. By establishing the relevant energy and exchange scales, this work expands the landscape of Nd pyrochlores where emergent gauge phenomena and exotic quasiparticles can be probed with quantitative precision.

Data availability–The data that support the findings of this study are openly available from the STFC ISIS Neutron and Muon Source at Ref. [61].

Acknowledgements– We thank Gang Chen and Arun Paramekanti for useful discussion. The synthesis, crystal growth, and crystallographic studies were performed at Clemson University and supported by DoE BES Award Number DE-SC0014271. B.R.O. (bulk property measurements and analysis) gratefully acknowledges support from the U.S. Department of Energy (DOE), Office of Science, Basic Energy Sciences, Materials Sciences and Engineering Division. Y.L., J.A.M.P., and A.A.A. acknowledge support from the U.S. Department of Energy (DOE), Office of Science, Basic Energy Sciences, Scientific User Facilities Division. We also thank the SNS X-ray Laboratory at ORNL for access to the Laue instrument used in sample co-alignment. Experiments at the ISIS Neutron and Muon Source were supported by beamtime allocations Grant No. RB2410211 from the Science and Technology Facilities Council.

This manuscript has been authored by UT-Battelle, LLC, under contract DE-AC05-00OR22725 with the U.S. Department of Energy (DOE). The U.S. government retains, and the publisher—by accepting the article for publication—acknowledges that the U.S. government retains a nonexclusive, paid-up, irrevocable, worldwide license to publish or reproduce the published form of this manuscript, or to allow others to do so, for U.S. government purposes. DOE will provide public access to these results of federally sponsored research in accordance with the DOE Public Access Plan (`https://www.energy.gov/doe-publicaccess-plan`).

* luoy1@ornl.gov
† aczelaa@ornl.gov

[1] J. S. Gardner, M. J. P. Gingras, and J. E. Greedan, Reviews of Modern Physics **82**, 53 (2010).
[2] E. M. Smith, E. Lhotel, S. Petit, and B. D. Gaulin, Annual Review of Condensed Matter Physics **16**, 387 (2025).
[3] L. Balents, Nature **464**, 199 (2010).
[4] L. Savary and L. Balents, Reports on Progress in Physics **80**, 016502 (2017), arXiv:1601.03742 [cond-mat.str-el].
[5] S. T. Bramwell, M. J. Harris, B. C. den Hertog, M. J. P. Gingras, J. S. Gardner, D. F. McMorrow, A. R. Wildes, A. L. Cornelius, J. D. M. Champion, R. G. Melko, and T. Fennell, Phys. Rev. Lett. **87**, 047205 (2001).
[6] B. C. den Hertog and M. J. P. Gingras, Physical Review Letters **84**, 3430 (2000).
[7] A. P. Ramirez, A. Hayashi, R. J. Cava, R. Siddharthan, and B. Shastry, Nature **399**, 333 (1999).

[8] T. Fennell, P. P. Deen, A. R. Wildes, K. Schmalzl, D. Prabhakaran, A. T. Boothroyd, R. J. Aldus, D. F. McMorrow, and S. T. Bramwell, Science **326**, 415 (2009).

[9] L. Savary and L. Balents, Physical Review Letters **108**, 037202 (2012).

[10] J. Gaudet, E. M. Smith, J. Dudemaine, J. Beare, C. R. C. Buhariwalla, N. P. Butch, M. B. Stone, D. R. Yahne, K. A. Ross, C. A. Marjerrison, J. D. Garrett, G. M. Luke, A. D. Bianchi, and B. D. Gaulin, Phys. Rev. Lett. **122**, 187201 (2019).

[11] A. Bhardwaj, S. Zhang, H. Yan, R. Moessner, A. H. Nevidomskyy, and H. J. Changlani, npj Quantum Materials **7**, 51 (2022).

[12] B. Gao, T. Chen, D. W. Tam, C. Huang, K. Sasmal, D. T. Adroja, F. Ye, H. Cao, G. Sala, M. B. Stone, C. Baines, J. A. T. Verezhak, H. Hu, J. Chung, X. Xu, S. Cheong, M. Nallaiyan, S. Spagna, M. B. Maple, A. H. Nevidomskyy, E. Morosan, G. Chen, and P. Dai, Nature Physics **15**, 1052 (2019).

[13] E. M. Smith, O. Benton, D. R. Yahne, B. Placke, R. Schäfer, J. Gaudet, J. Dudemaine, A. Fitterman, J. Beare, A. R. Wildes, S. Bhattacharya, T. DeLazzer, C. R. C. Buhariwalla, N. P. Butch, R. Movshovich, J. D. Garrett, C. A. Marjerrison, J. P. Clancy, E. Kermarrec, G. M. Luke, A. D. Bianchi, K. A. Ross, and B. D. Gaulin, Physical Review X **12**, 021015 (2022).

[14] E. M. Smith, R. Schäfer, J. Dudemaine, B. Placke, B. Yuan, Z. Morgan, F. Ye, R. Moessner, O. Benton, A. D. Bianchi, and B. D. Gaulin, Phys. Rev. X **15**, 021033 (2025).

[15] B. Gao, F. Desrochers, D. W. Tam, D. M. Kirschbaum, P. Steffens, A. Hiess, D. H. Nguyen, Y. Su, S.-W. Cheong, S. Paschen, *et al.*, Nature Physics , 1 (2025).

[16] R. Sibille, N. Gauthier, E. Lhotel, V. Porée, V. Pomjakushin, R. A. Ewings, T. G. Perring, J. Ollivier, A. R. Wildes, C. Ritter, T. C. Hansen, D. A. Keen, G. J. Nilsen, L. Keller, S. Petit, and T. Fennell, Nature Physics **16**, 546 (2020).

[17] V. Porée, H. Yan, F. Desrochers, S. Petit, E. Lhotel, M. Appel, J. Ollivier, Y. Kim, A. Nevidomskyy, and R. Sibille, Nature Physics **21**, 83 (2025).

[18] D. R. Yahne, B. Placke, R. Schäfer, O. Benton, R. Moessner, M. Powell, J. W. Kolis, C. M. Pasco, A. F. May, M. D. Frontzek, E. M. Smith, B. D. Gaulin, S. Calder, and K. A. Ross, Phys. Rev. X **14**, 10.1103/PhysRevX.14.011005 (2024).

[19] V. Porée, A. Bhardwaj, E. Lhotel, S. Petit, N. Gauthier, H. Yan, V. Pomjakushin, J. Ollivier, J. A. Quilliam, A. H. Nevidomskyy, H. J. Changlani, and R. Sibille, arXiv preprint (2023), arXiv:2305.08261.

[20] E. M. Smith, A. Fitterman, R. Schäfer, B. Placke, A. Woods, S. Lee, S. H.-Y. Huang, J. Beare, S. Sharma, D. Chatterjee, *et al.*, Physical Review Letters **135**, 086702 (2025).

[21] J. Xu, V. K. Anand, A. K. Bera, M. Frontzek, D. L. Abernathy, N. Casati, K. Siemensmeyer, and B. Lake, Physical Review B **92**, 224430 (2015), publisher Copyright: © 2015 American Physical Society.

[22] E. Lhotel, S. Petit, S. Guitteny, O. Florea, M. C. Hatnean, C. Colin, E. Ressouche, M. R. Lees, and G. Balakrishnan, Physical Review Letters **115**, 197202 (2015).

[23] S. Petit, E. Lhotel, B. Canals, M. Ciomaga Hatnean, J. Ollivier, H. Mutka, E. Ressouche, A. R. Wildes, M. R. Lees, and G. Balakrishnan, Nature Physics **12**, 746 (2016).

[24] J. Xu, C. Balz, C. Baines, H. Luetkens, and B. Lake, Physical Review B **94**, 064425 (2016).

[25] O. Benton, Physical Review B **94**, 104430 (2016).

[26] É. Lhotel, S. Petit, M. Ciomaga Hatnean, J. Ollivier, H. Mutka, E. Ressouche, M. R. Lees, and G. Balakrishnan, Nature Communications **9**, 3786 (2018).

[27] J. Xu, A. T. M. N. Islam, I. N. Glavatskyy, M. Reehuis, J.-U. Hoffmann, and B. Lake, Physical Review B **98**, 060408 (2018).

[28] J. Xu, O. Benton, V. K. Anand, A. T. M. N. Islam, T. Guidi, G. Ehlers, E. Feng, Y. Su, A. Sakai, P. Gegenwart, and B. Lake, Physical Review B **99**, 144420 (2019), arXiv:1904.07819.

[29] J. Xu, O. Benton, A. T. M. N. Islam, T. Guidi, G. Ehlers, and B. Lake, Physical Review Letters **124**, 097203 (2020), arXiv:1907.11056.

[30] M. Léger, E. Lhotel, M. Ciomaga Hatnean, J. Ollivier, A. R. Wildes, S. Raymond, E. Ressouche, G. Balakrishnan, and S. Petit, Physical Review Letters **126**, 247201 (2021).

[31] M. Léger, F. Vayer, M. Ciomaga Hatnean, F. Damay, C. Decorse, D. Berardan, B. Fåk, J. Zanotti, Q. Berrod, J. Ollivier, J. P. Embs, T. Fennell, D. Sheptyakov, S. Petit, and E. Lhotel, Physical Review B **109**, 224416 (2024).

[32] V. Anand, A. Bera, J. Xu, T. Herrmannsdörfer, C. Ritter, and B. Lake, Physical Review B **92**, 184418 (2015).

[33] V. K. Anand, D. L. Abernathy, D. T. Adroja, A. D. Hillier, P. K. Biswas, and B. Lake, Physical Review B **95**, 224420 (2017).

[34] A. Samartzis, J. Xu, V. Anand, A. Islam, J. Ollivier, Y. Su, and B. Lake, Physical Review B **106**, L100401 (2022).

[35] A. Bertin, P. D. de Réotier, B. Fåk, C. Marin, A. Yaouanc, A. Forget, D. Sheptyakov, B. Frick, C. Ritter, A. Amato, C. Baines, and P. J. C. King, Physical Review B **92**, 144423 (2015).

[36] P. D. de Réotier, A. Yaouanc, A. Maisuradze, A. Bertin, P. J. Baker, A. D. Hillier, and A. Forget, Physical Review B **95**, 134420 (2017).

[37] A. M. Hallas, A. M. Arevalo-Lopez, A. Z. Sharma, T. Munsie, J. P. Attfield, C. R. Wiebe, and G. M. Luke, Physical Review B **91**, 104417 (2015).

[38] D. Swarnakar, Y. Jana, J. Alam, and S. Nandi, Physica B: Condensed Matter **521**, 93 (2017).

[39] B. Z. Malkin, T. T. A. Lummen, P. H. M. Van Loosdrecht, G. Dhalenne, and A. R. Zakirov, Journal of Physics: Condensed Matter **22**, 276003 (2010).

[40] S. Singh, S. Saha, S. K. Dhar, R. Suryanarayanan, A. K. Sood, and A. Revcolevschi, Physical Review B **77**, 054408 (2008).

[41] C. Mauws, A. M. Hallas, G. Sala, A. A. Aczel, P. M. Sarte, J. Gaudet, D. Ziat, J. A. Quilliam, J. A. Lussier, M. Bieringer, *et al.*, Physical Review B **98**, 100401 (2018).

[42] V. Peçanha-Antonio, E. Feng, X. Sun, D. Adroja, H. C. Walker, A. S. Gibbs, F. Orlandi, Y. Su, and T. Brückel, Physical Review B **99**, 134415 (2019).

[43] Y.-P. Huang, G. Chen, and M. Hermele, Physical review letters **112**, 167203 (2014).

[44] J. G. Rau and M. J. P. Gingras, Annual Review of Condensed Matter Physics **10**, 357 (2019), review article, arXiv:1806.09638.

[45] Y.-D. Li and G. Chen, Physical Review B **95**, 041106 (2017).

[46] X.-P. Yao, Y.-D. Li, and G. Chen, Physical Review Research **2**, 013334 (2020).

[47] O. Benton, Physical Review B **102**, 104408 (2020).

[48] A. S. Patri, M. Hosoi, and Y. B. Kim, Physical Review Research **2**, 023253 (2020).

[49] M. E. Brooks-Bartlett, S. T. Banks, L. D. C. Jaubert, A. Harman-Clarke, and P. C. W. Holdsworth, Physical Review X **4**, 011007 (2014).

[50] É. Lhotel, L. D. C. Jaubert, and P. C. W. Holdsworth, Journal of Low Temperature Physics **201**, 710 (2020).

[51] C. Mauws, N. Hiebert, M. L. Rutherford, H. D. Zhou, Q. Huang, M. B. Stone, N. P. Butch, Y. Su, E. S. Choi, Z. Yamani, *et al.*, Journal of Physics: Condensed Matter **33**, 245802 (2021).

[52] A. Scheie, M. Sanders, X. Gui, Y. Qiu, T. R. Prisk, R. J. Cava, and C. Broholm, Physical Review B **104**, 134418 (2021).

[53] G. Chen, Phys. Rev. Research **5**, L032027 (2023).

[54] S. Gomez, P. Sarte, M. Zelensky, A. Hallas, B. Gonzalez, K. Hong, E. Pace, S. Calder, M. Stone, Y. Su, *et al.*, Physical Review B **103**, 214419 (2021).

[55] A. Bertin, *Geometrical Frustration and Quantum Origin of Spin Dynamics*, Phd thesis, Université Grenoble Alpes, Grenoble, France (2015).

[56] M. Powell, L. D. Sanjeewa, C. D. McMillen, K. A. Ross, C. L. Sarkis, and J. W. Kolis, Crystal Growth & Design **19**, 4920 (2019).

[57] H. Fukazawa, R. G. Melko, R. Higashinaka, Y. Maeno, and M. J. P. Gingras, Physical Review B **65**, 054410 (2002).

[58] H. Yan, R. Pohle, and N. Shannon, Phys. Rev. B **98**, 140402(R) (2018), arXiv:1806.08520 [cond-mat.str-el].

[59] X. Bai, S.-S. Zhang, Z. Dun, H. Zhang, Q. Huang, H. Zhou, M. B. Stone, A. I. Kolesnikov, F. Ye, C. D. Batista, *et al.*, Nature Physics **17**, 467 (2021).

[60] S. Carretta, P. Santini, R. Caciuffo, and G. Amoretti, Physical review letters **105**, 167201 (2010).

[61] Yi Luo et al., Neutron spectroscopy study of the dipolar–octupolar pyrochlore $Nd_2Sn_2O_7$ (2024), dataset released under the CC-BY-4.0 license.

[62] R. A. Ewings, A. Buts, M. D. Le, J. van Duijn, I. Bustinduy, and T. G. Perring, Nuclear Instruments and Methods in Physics Research Section A **834**, 132 (2016).

[63] Y. Okamoto, G. J. Nilsen, J. P. Attfield, and Z. Hiroi, Physical Review Letters **110**, 097203 (2013).

[64] K. Baroudi, B. D. Gaulin, S. H. Lapidus, J. Gaudet, and R. J. Cava, Physical Review B **92**, 024110 (2015).

[65] R. L. Smit, S. Keupert, O. Tsyplyatyev, P. A. Maksimov, A. L. Chernyshev, and P. Kopietz, Physical Review B **101**, 054424 (2020).

[66] J. H. P. Colpa, Physica A: Statistical Mechanics and its Applications **93**, 327 (1978).

[67] K. Kang, D. G. Cahill, and A. Schleife, Physical Review B **107**, 064412 (2023).

Supplemental Material for "Magnetic Moment Fragmentation in an All-in–All-out Pyrochlore $Nd_2Sn_2O_7$"

S1. METHODS AND SAMPLE INFORMATION

Single crystals of $Nd_2Sn_2O_7$ were grown by spontaneous nucleation using a high-temperature, high-pressure hydrothermal technique [56]. Stoichiometric amounts of the corresponding dry oxides and a 5 M CsF/CsOH mineralizer solution were loaded into fine silver ampoules in a 1:4 g:mL ratio. The ampoules were weld-sealed, placed in a Tuttle-seal autoclave, and supplemented with deionized water to provide adequate counterpressure (typically ∼100 MPa). The sealed autoclaves were heated with ceramic band heaters to generate a cold–hot gradient of 670–680 °C for 14–21 days, promoting crystal growth via convective transport of the nutrient solution from the hotter dissolution zone to the cooler crystallization zone. After the reaction, the autoclaves were cooled in air, and the ampoules were collected, opened, and vacuum-filtered. The recovered product was washed with deionized water, dried with acetone, and yielded well-faceted purple octahedral crystals, typically 1–20 mg in mass and millimeter-sized [Fig. S1(a–c)]. A single crystal $Nd_2Sn_2O_7$ specimen (~ 0.1 mm^3) was used for single-crystal X-ray diffraction (SCXRD) measurements on a Bruker Venture D8 diffractometer using Mo Kα radiation source at room temperature, and the refined structural parameters are listed in Table SI.

Heat-capacity measurements from 250 K to 1.8 K and in the dilution-refrigerator temperature range were performed using the Quantum Design heat-capacity option on a 9 T PPMS. The lattice contribution was estimated from nonmagnetic, hydrothermally grown $La_2Sn_2O_7$ and subtracted from the raw data. The combined data is shown in Fig. 1(b). The slight upturn of C_p below approximately 0.25 K may originate from the onset of a nuclear contribution, similar to that reported for $Nd_2Zr_2O_7$ [28]. In this regime ($T \lesssim 0.25$ K), the PPMS relaxation method does not return a reliable thermal time constant, a situation that can arise when a nuclear Schottky term grows rapidly and the effective heat capacity changes during the measurement. This instability might lead to nonphysical C_p values, and therefore we do not perform quantitative fitting below 0.25 K.

DC magnetic susceptibility measurements from 300-1.8 K were measured with a Magnetic Property Measurement System (MPMS3). Additional measurements from 4 K-400 mK were performed with the Quantum Design iHe-3 He^3 insert for the MPMS3. ^{4}He-range susceptibility was recorded on a ∼1 mg pulverized single crystal. ^{3}He-range measurements used 29.1 mg of pulverized single-crystal $Nd_2Sn_2O_7$ in a 100 Oe field. The resulting datasets were normalized and combined. Magnetization versus field measurements at $T = 2$ K were performed on single-crystal $Nd_2Sn_2O_7$ samples with masses of ∼1.50 mg ($H \parallel [100]$), ∼0.93 mg ($H \parallel [111]$), and ∼1.36 mg ($H \parallel [110]$). The induced magnetic moments M at the maximum applied field of $\mu_0 H = 7$ T were determined to be 1.67 μ_B/Nd^{3+}, 1.43 μ_B/Nd^{3+}, and 1.28 μ_B/Nd^{3+} for fields along the [100], [111], and [110] directions, respectively. For comparison, the expected saturated moments in a pyrochlore lattice with local ⟨111⟩ Ising anisotropy and effective ferromagnetic (FM) nearest-neighbor coupling are $g_J J/\sqrt{3}$ for [100], $g_J J/2$ for [111], and $g_J J/\sqrt{6}$ for [110] [57]. The observed ordering of induced moments (largest to smallest) and their relative ratios are consistent with these theoretical expectations for a magnetic pyrochlore with easy-axis anisotropy [57]. Small quantitative deviations may originate from slight sample misalignment during mounting, uncertainties in mass due to residual impurity phases, or incomplete saturation at $\mu_0 H = 7$ T.

For single-crystal neutron scattering experiments, 153 individual crystals were co-aligned and affixed to one oxygen-free copper plate using GE varnish, covering a rectangular area of approximately 2.0 cm (vertical) × 1.0 cm (horizontal) on each side [Fig. S1(a)], with the (HHL) plane lying in the horizontal scattering plane. The assembly behaved effectively as a single, slightly broadened crystal grain with a total mass of ∼0.93 g and an estimated mosaic spread of ∼5° full width at half maximum (FWHM).

Inelastic neutron scattering measurements were carried out on the cold neutron chopper spectrometer LET at the ISIS Neutron and Muon Source, RAL, UK. Data were collected at $T = 0.25$ K and $T = 10$ K using simultaneous incident energies of $E_i = 2.19$, 3.7, 7.51, and 22.7 meV, enabled by the multi-chopper system. The chopper configuration was 120 Hz/120 Hz (choppers 5 and 3), 60 Hz/60 Hz (choppers 1 and 4), with chopper 2 phased to 8800 at 10 Hz. These settings provided elastic-line energy resolutions (FWHM) of approximately 0.07, 0.15, 0.40, and 2.1 meV for $E_i = 2.19$, 3.7, 7.51, and 22.7 meV, respectively. For the $E_i = 2.19$ meV data shown in the main text, the accessible energy window is estimated to be ~ 0.09 meV based on 3σ, with $\sigma = \text{FWHM}/2.355$. This serves as a reasonable lower limit above which the elastic background does not dominate. The sample was rotated about the vertical $[1\bar{1}0]$ axis over a total range of 180° in 1° steps. Data reduction and analysis were performed using the Horace software suite [62]. Measurements with $E_i = 22.7$ meV were specifically used to assess the sample mosaicity and alignment [Fig. S1(d–h)]. No background subtraction was applied to any of the data presented in the main text or in the Supplemental Material, except in Fig. S3(b), where it is explicitly stated that the 0.25 K − 10 K difference is shown.

Figure S2(a) shows a false-color intensity map of the

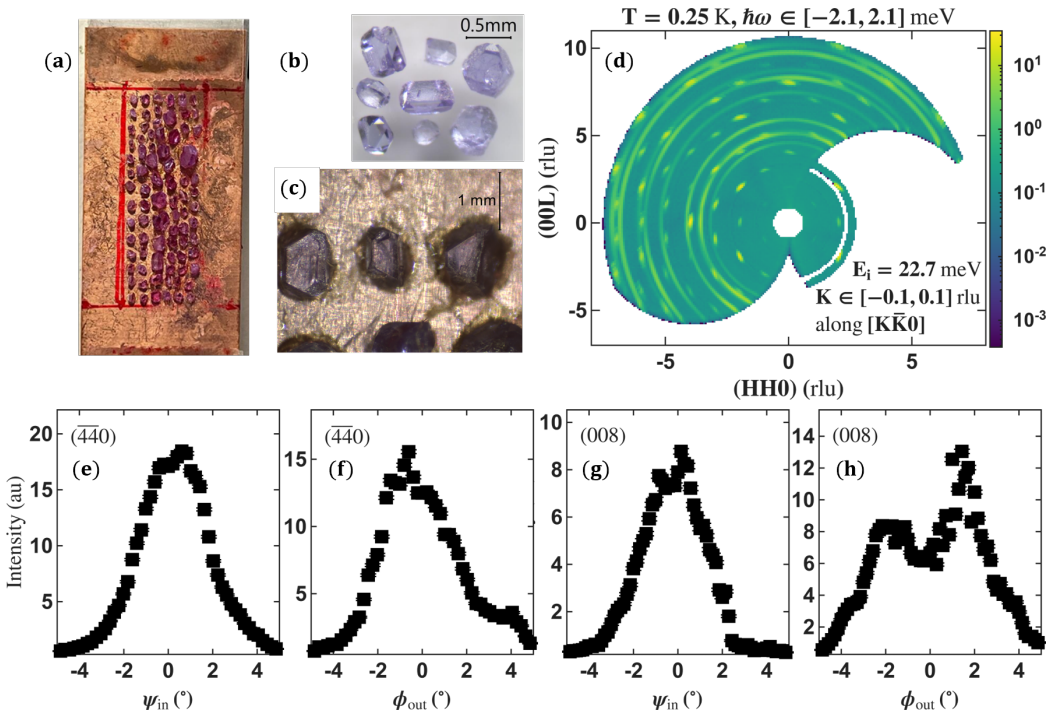

FIG. S1. (a) Photograph of a portion of the co-aligned single-crystal $Nd_2Sn_2O_7$ array (total mass ∼0.93 g), with the vertical axis approximately aligned along the $[1\bar{1}0]$ crystallographic direction. (b) Optical microscopy image of a representative single crystal. (c) Optical microscopy image of crystals affixed to the copper plate within the co-aligned array shown in (a). (d) False-color intensity map of the (HHL) plane of the co-aligned $Nd_2Sn_2O_7$ crystal array, collected at $T = 0.25$ K on the cold neutron multi-chopper spectrometer LET with incident energy $E_i = 22.7$ meV. The map displays the elastic channel integrated over energy transfer $[-2.1, 2.1]$ meV and within ±0.1 rlu along the $[K\bar{K}0]$ direction. The data reveal a single, slightly broadened crystal grain with an estimated mosaicity of ∼5° (FWHM), further illustrated in (e–h). (e–h) Transverse cuts through the Bragg peaks $\mathbf{Q} = (\bar{4}\bar{4}0)$ and $\mathbf{Q} = (008)$ along the in-plane directions [001] and [110], respectively, as well as the out-of-plane direction $[K\bar{K}0]$, measured at $T = 0.3$ K. Horizontal axes are expressed in angular units ψ_{in} (in-plane) and ϕ_{out} (out-of-plane), normalized to $|\mathbf{Q}|$. Data are integrated within ±0.09 Å^{-1} in the perpendicular $\mathbf{Q}$ directions.

TABLE SI. Atomic positions and anisotropic displacement parameters of single-crystal $Nd_2Sn_2O_7$ collected at $T = 300$ K from SCXRD measurement.

Lattice parameter (Å): 10.57170(17)									Space group: $Fd\bar{3}m$
Atom (Wyckoff)	x	y	z	u_{11}	u_{22}	u_{33}	u_{23}	u_{13}	u_{12}
Sn (16c)	0.5	0.75	0.25	0.0166(8)	0.0166(8)	0.0166(8)	0.00007(10)	-0.00007(10)	-0.00007(10)
Nd (16d)	0.5	0.5	0.5	0.0187(7)	0.0187(7)	0.0187(7)	-0.00094(8)	-0.00094(8)	-0.00094(8)
O (8b)	0.625	0.625	0.625	0.0203(17)	0.0203(17)	0.0203(17)	0	0	0
O (48f)	0.4182(3)	0.625	0.125	0.0187(19)	0.0196(13)	0.0196(13)	-0.0039(14)	0	0

(HHL) plane at the elastic line, collected with $E_i = 3.7$ meV at $T = 0.25$ K, where clear intensity is observed at the nominally forbidden (002) position. Constant-Q energy cuts at several zone centers are presented in Fig. S2(b–d) for $E_i = 2.19$ meV and in Fig. S2(e–g) for $E_i = 3.7$ meV. At both incident energies and temperatures, finite intensity is detected at (002) [Fig. S2(b,e)]. A temperature-dependent enhancement of this signal is evident only in the $E_i = 2.19$ meV data, where the intensity at $T = 0.25$ K exceeds that at $T = 10$ K [Fig. S2(b)], while the corresponding difference in the $E_i = 3.7$ meV data is negligible [Fig. S2(e)]. The (002) reflection is also observed in measurements with $E_i = 7.59$ meV (not shown), with nearly identical intensity at both $T = 0.25$ K and $T = 10$ K. Notably, the (002) reflection is absent in the SCXRD data collected at $T = 300$ K and $T = 100$ K. The refinement at $T = 300$ K confirms a pyrochlore structure with space group $Fd\bar{3}m$ [Table SI]. A genuine (002) reflection can only arise if the crystal symmetry is lowered from the pyrochlore space group $Fd\bar{3}m$, such as through a transition to the subgroup $F\bar{4}3m$ [63]. However, heat-capacity measurements on the single-crystal $Nd_2Sn_2O_7$ sample over the temperature range [5,250] K [Fig. S3(a)] show no indication of any structural transition. Taken together, these observations suggest that the observed (002) reflection is more likely of

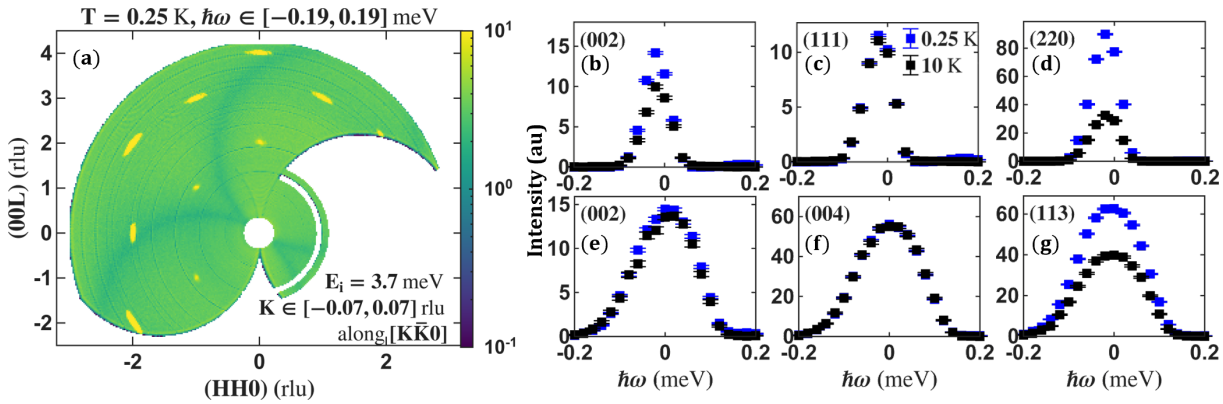

FIG. S2. (a) False-color intensity map of the (HHL) plane of the co-aligned $Nd_2Sn_2O_7$ crystal array, collected at $T = 0.25$ K on the cold neutron multi-chopper spectrometer LET with incident energy $E_i = 3.7$ meV. The map shows the elastic channel integrated over an energy range of $[-0.2, 0.2]$ meV and within ± 0.07 rlu along the $[K\bar{K}0]$ direction. (b–g) Constant-Q energy cuts at the positions indicated in each panel, integrated over $[-0.1, 0.1]$ rlu along each principal reciprocal-space direction. Blue curves correspond to data collected at $T = 0.25$ K and black curves to $T = 10$ K. Panels (b–d) were measured with $E_i = 2.19$ meV, while panels (e–g) were measured with $E_i = 3.7$ meV. Panels (b–g) show data from Bragg peaks in the (HHL) plane, symmetrized using the $Fd\bar{3}m$ space-group symmetry.

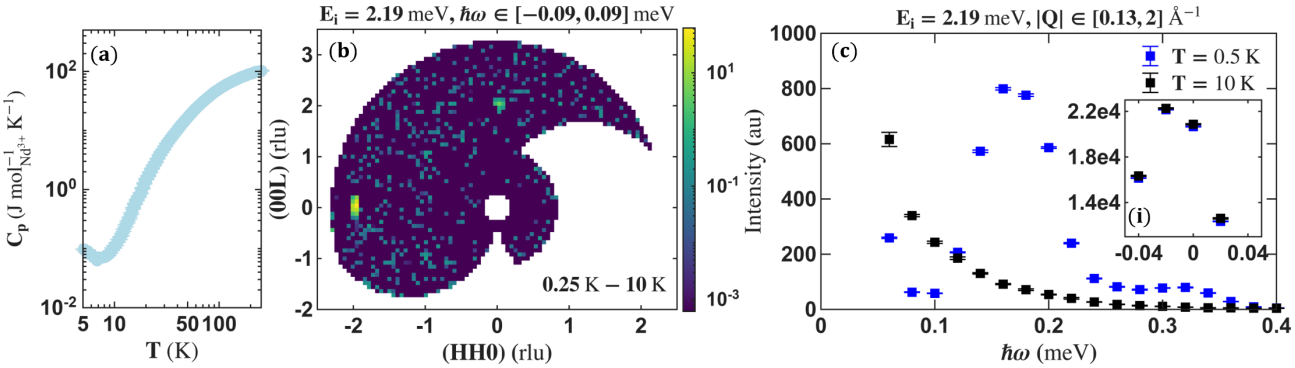

FIG. S3. (a) Heat capacity C_p versus temperature T for single-crystal $Nd_2Sn_2O_7$ sample in the temperature range $T \in [5, 250]$ K, with no background subtraction from hydrothermally grown $La_2Sn_2O_7$ crystals. (b) False-color intensity map of the (HHL) plane for the co-aligned $Nd_2Sn_2O_7$ crystal array, measured with incident energy $E_i = 2.19$ meV. The map shows the difference $I(0.25\,\mathrm{K}) - I(10\,\mathrm{K})$ in the elastic channel, integrated over $[-0.09, 0.09]$ meV and within ± 0.07 rlu along $[K\bar{K}0]$. (c) Powder-averaged intensity versus energy transfer $\hbar\omega$ at $T = 0.25$ and 10 K for $E_i = 2.19$ meV, integrated along $[K\bar{K}0]$ with $K \in [-0.07, 0.07]$ rlu and over $Q \in [0.13, 2]$ Å^{-1} within the (HHL) plane. Inset (i) shows the corresponding elastic intensity.

extrinsic origin, such as multiple scattering, rather than a genuine cooling-induced lattice distortion. Similar (002) reflections have been reported in $Ho_2Ti_2O_7$, $Yb_2Ti_2O_7$, and $Er_2Ti_2O_7$, and were attributed to multiple scattering from strong allowed Bragg reflections [64].

In Fig. S2(c,d,f,g), comparison of the $T = 0.25$ K and $T = 10$ K datasets reveals pronounced magnetic Bragg intensity at (220) and (113), with essentially no additional magnetic signal at (111) and (004). This pattern is consistent with the noncoplanar all-in–all-out (AIAO) magnetic structure reported in Ref. [35].

S2. ADDITIONAL NEUTRON SPECTROSCOPY DATA

The primary data sets presented in the main text were acquired with incident energy $E_i = 2.19$ meV. Figure S3(b) shows the (HHL) Q-map at $T = 0.25$ K in the elastic channel within resolution (FWHM ≈ 0.07 meV), integrated over $[-0.09, 0.09]$ meV, with the $T = 10$ K data subtracted as an elastic background. No residual magnetic diffuse-scattering signal is observed in the elastic channel. The corresponding powder-averaged intensity within the (HHL) plane at $T = 0.25$ and 10 K is shown in Fig. S3(c), which reveals only the spin-wave excitation discussed in the main text, confined to $\hbar\omega \in [0.1, 0.4]$ meV.

Additional measurements at $E_i = 3.7$, 7.51, and

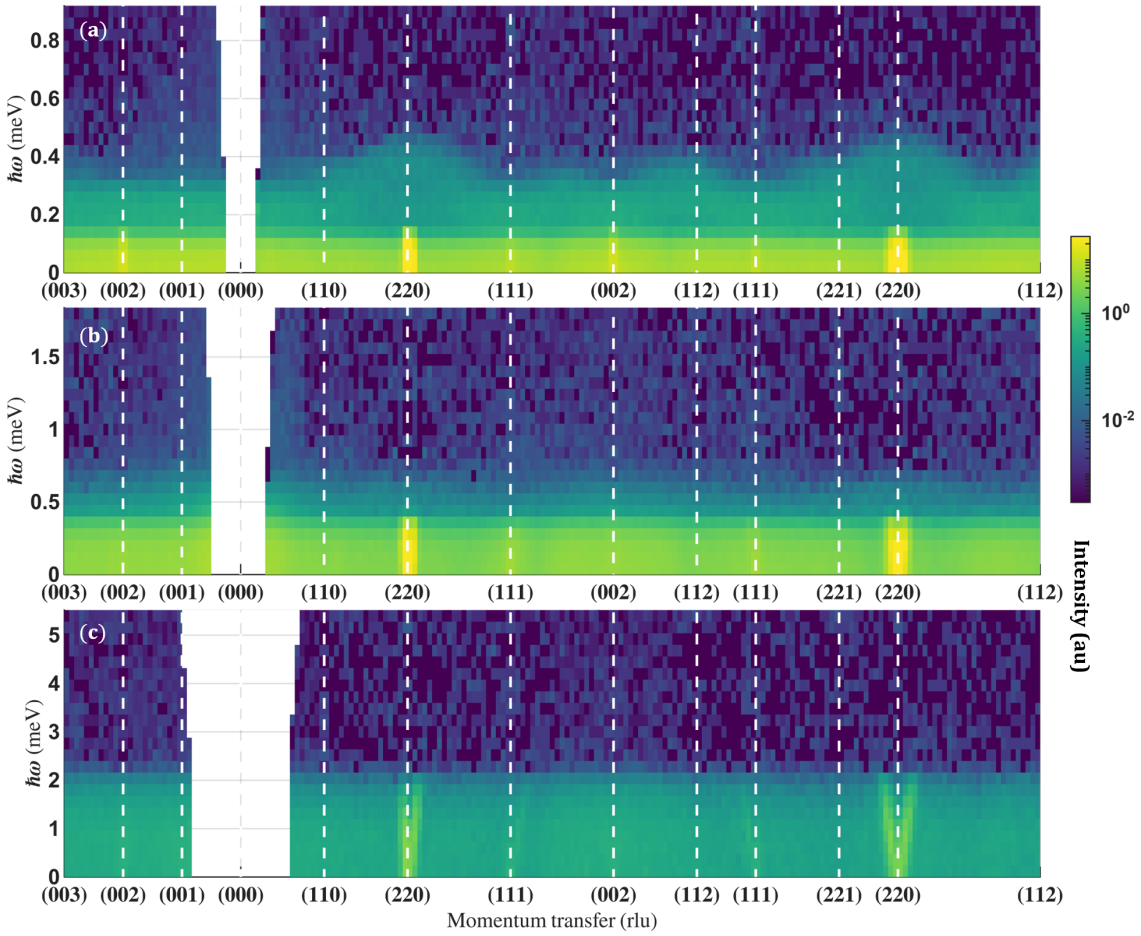

FIG. S4. False color map of inelastic scattering intensity $S(\mathbf{Q},\omega)$ versus energy transfer $\hbar\omega$ and momentum transfer Q along a path connecting the labeled high symmetry points. Data were taken at $T = 0.25$ K with incident energy (a) $E_i = 3.7$ meV,(b) 7.51 meV , and (c) 22.7 meV on the LET spectrometer, integrated over a perpendicular momentum window of ± 0.1 Å^{-1}.

22.7 meV, all at $T = 0.25$ K, are shown in Fig. S4. No discernible magnetic signal is observed in the combined range 0.5–5 meV across all panels. The intensity at (220) for $E_i = 22.7$ meV below $\hbar\omega = 2$ meV is attributable to the elastic-line tail from the finite energy resolution (FWHM ≈ 2.1 meV).

The $T = 10$ K neutron spectrum collected with $E_i = 2.19$ meV is shown in Fig. S5(b), alongside the $T = 0.25$ K data in Fig. S5(a) (also presented in Fig. 2(a)). It is clear from Fig. S5(b), Fig. 3 and Fig. S6 that the spin-wave excitations visible at 0.25 K are entirely absent at 10 K. For this reason, no background subtraction was applied to the data presented in the main text.

S3. DETAILS OF SPIN-WAVE MODEL

S3.1 LSWT Hamiltonian

We closely follow the theoretical approach introduced in Ref. [25] for the isostructural sister compound $Nd_2Zr_2O_7$. The ground state doublet of Nd^{3+} in $Nd_2Sn_2O_7$ has a dipolar-octupolar character. A natural basis choice, $|\uparrow\rangle$ and $|\downarrow\rangle$, diagonalizes the angular momentum operator $\mathbf{J}$ along the local z-axis, which coincides with the C_3 symmetry axis at each Nd^{3+} site. Following Ref. [43], the local axes are defined as:

$$\begin{aligned}
\hat{\mathbf{z}}_1 &= \frac{1}{\sqrt{3}}(1,1,1), & \hat{\mathbf{y}}_1 &= \frac{1}{\sqrt{2}}(0,1,-1),\\
\hat{\mathbf{z}}_2 &= \frac{1}{\sqrt{3}}(1,-1,-1), & \hat{\mathbf{y}}_2 &= \frac{1}{\sqrt{2}}(-1,0,-1),\\
\hat{\mathbf{z}}_3 &= \frac{1}{\sqrt{3}}(-1,1,-1), & \hat{\mathbf{y}}_3 &= \frac{1}{\sqrt{2}}(-1,-1,0),\\
\hat{\mathbf{z}}_4 &= \frac{1}{\sqrt{3}}(-1,-1,1), & \hat{\mathbf{y}}_4 &= \frac{1}{\sqrt{2}}(-1,1,0),
\end{aligned} \tag{3}$$

and $\hat{x}_i = \hat{y}_i \times \hat{z}_i$ corresponding to the four Nd^{3+} ions located at fractional coordinates $\hat{\mathbf{r}}_1 = (0.5, 0.5, 0.5)$, $\hat{\mathbf{r}}_2 = (0.5, 0.75, 0.75)$, $\hat{\mathbf{r}}_3 = (0.75, 0.5, 0.75)$, and $\hat{\mathbf{r}}_4 = (0.75, 0.75, 0.5)$ in the unit cell. Only the angular momentum component along $\hat{z}$, $\hat{J}_z$, has a non-zero matrix

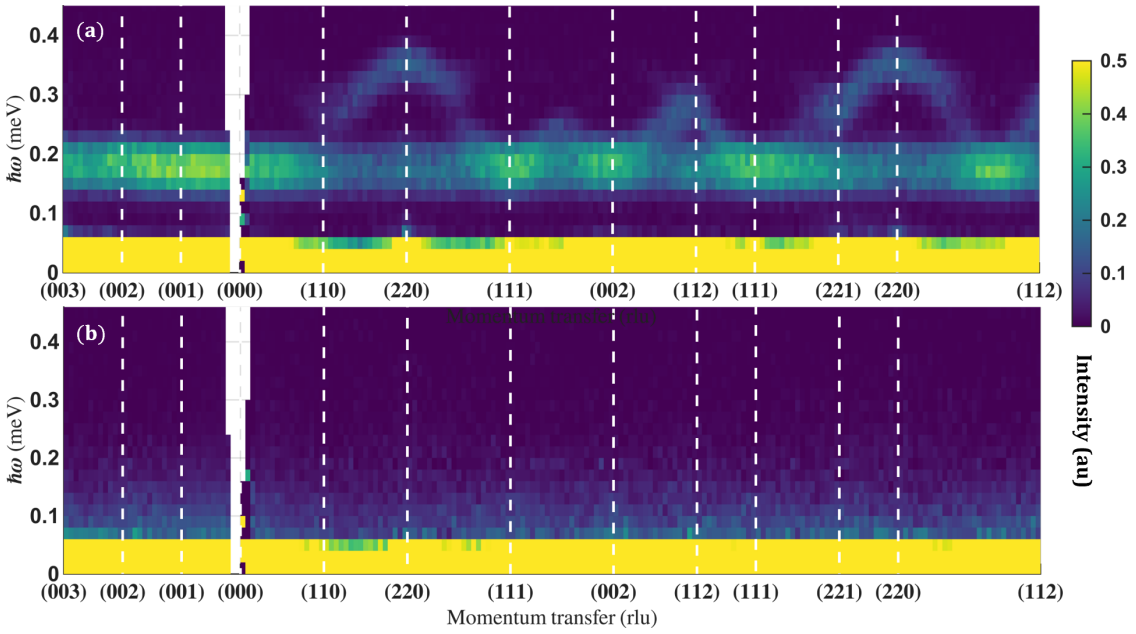

FIG. S5. False color map of inelastic scattering intensity $S(\mathbf{Q},\omega)$ versus energy transfer $\hbar\omega$ and momentum transfer Q along a path connecting the labeled high symmetry points. Data were taken at (a) $T = 0.25$ K and (b) $T = 10$ K with incident energy $E_i = 2.19$ meV on the LET spectrometer, integrated over a perpendicular momentum window of ± 0.1 Å^{-1}, and not symmetrized.

element within the ground state doublet, while $\hat{J}_x$ and $\hat{J}_y$ have vanishing matrix elements [21, 22].

We introduce pseudospin-1/2 operators $(\tau_i^x, \tau_i^y, \tau_i^z)$ at each site i, such that the magnetic moment is given by $\mathbf{m}_i = g_z \mu_B \tau_i^z$, where g_z is the effective g-factor along the local $\hat{z}_i$ direction. The symmetry-allowed nearest-neighbor exchange Hamiltonian is:

$$\mathcal{H}_{\text{ex}}^{\text{DO}} = \sum_{\langle ij \rangle} \big[J_x \tau_i^x \tau_j^x + J_y \tau_i^y \tau_j^y + J_z \tau_i^z \tau_j^z + J_{xz} (\tau_i^x \tau_j^z + \tau_i^z \tau_j^x) \big]. \tag{4}$$

where $\langle ij \rangle$ runs through all pairs of nearest neighbor Nd^{3+}. A global rotation of the pseudospin components $\tau_i^\alpha \to \tilde{\tau}_i^{\tilde{\alpha}}$,

$$\begin{aligned} \tilde{\tau}_i^{\tilde{x}} &= \cos(\vartheta)\, \tau_i^x + \sin(\vartheta)\, \tau_i^z, \quad \tilde{\tau}_i^{\tilde{y}} = \tau_i^y, \\ \tilde{\tau}_i^{\tilde{z}} &= \cos(\vartheta)\, \tau_i^z - \sin(\vartheta)\, \tau_i^x, \quad \tan(\vartheta) = \frac{2J_{xz}}{J_x - J_z}, \end{aligned} \tag{5}$$

eliminates the J_{xz} term and yields an effective XYZ model:

$$\mathcal{H}_{\text{xyz}}^{\text{DO}} = \sum_{\langle ij \rangle} \left[\tilde{J}_x \tilde{\tau}_i^{\tilde{x}} \tilde{\tau}_j^{\tilde{x}} + \tilde{J}_y \tilde{\tau}_i^{\tilde{y}} \tilde{\tau}_j^{\tilde{y}} + \tilde{J}_z \tilde{\tau}_i^{\tilde{z}} \tilde{\tau}_j^{\tilde{z}} \right]. \tag{6}$$

The magnetic moment at each site i can then be decomposed as:

$$\mathbf{m}_i = g_z \mu_B \left[\cos(\vartheta)\, \mathbf{m}_i^{\tilde{z}} + \sin(\vartheta)\, \mathbf{m}_i^{\tilde{x}} \right], \tag{7}$$

where

$$\mathbf{m}_i^{\tilde{\alpha}} = \tilde{\tau}_i^{\tilde{\alpha}}\, \hat{z}_i, \qquad \alpha = x, z. \tag{8}$$

The τ_i^y (or $\tilde{\tau}_i^{\tilde{y}}$) component transforms as a magnetic octupole and does not contribute to the dipolar magnetic moment. Following Ref. [25], we identify the origin of magnetic moment fragmentation: the component $\mathbf{m}_i^{\tilde{z}}$ forms an "all-in, all-out" (AIAO) magnetic order, while fluctuations in $\mathbf{m}_i^{\tilde{x}}$ give rise to spin-wave excitations. The AIAO ground state is stabilized within the following parameter regime:

$$\tilde{J}_z < 0, \quad -|\tilde{J}_z| < \tilde{J}_x,\ \tilde{J}_y < 3|\tilde{J}_z|. \tag{9}$$

For linear spin-wave theory (LSWT), we apply Holstein-Primakoff (HP) transformation

$$\begin{aligned} \tilde{\tau}_i^{\tilde{z}} &= S - a_i^\dagger a_i \\ \tilde{\tau}_i^{+} \equiv \tilde{\tau}_i^{\tilde{x}} + i\tilde{\tau}_i^{\tilde{y}} &= \sqrt{2S - a_i^\dagger a_i}\ a_i \approx \sqrt{2S}\ a_i \\ \tilde{\tau}_i^{-} \equiv \tilde{\tau}_i^{\tilde{x}} - i\tilde{\tau}_i^{\tilde{y}} &= a_i^\dagger \sqrt{2S - a_i^\dagger a_i} \approx \sqrt{2S}\ a_i^\dagger \end{aligned} \tag{10}$$

where $S = 1/2$ and the HP bosons a_i satisfys $[a_i, a_j^\dagger] = \delta_{ij}$. Substituting Eq.10 into Eq.6 gives the LSWT Hamiltonian:

$$\begin{aligned} \mathcal{H}_{\text{LSWT}}^{\text{DO}} &= -3N|\tilde{J}_z|S^2 + 6|\tilde{J}_z|S \sum_i a_i^\dagger a_i \\ &+ \frac{S}{2} \sum_{\langle ij \rangle} (a_i^\dagger, a_i) \begin{pmatrix} \tilde{J}_x + \tilde{J}_y & \tilde{J}_x - \tilde{J}_y \\ \tilde{J}_x - \tilde{J}_y & \tilde{J}_x + \tilde{J}_y \end{pmatrix} \begin{pmatrix} a_j \\ a_j^\dagger \end{pmatrix} \end{aligned} \tag{11}$$

We now perform a lattice Fourier transformation on the bosonic operators a_i and $a_i^\dagger$, where each site i is labeled by the unit cell index n and one of the four sublattices m within a tetrahedron:

$$\begin{aligned} a_{n,m}^\dagger &= \frac{1}{\sqrt{N}} \sum_{\mathbf{k}} a_{\mathbf{k}m}^\dagger \exp(i\mathbf{k}\cdot(\mathbf{R}_n + \mathbf{r}_m)) \\ a_{n,m} &= \frac{1}{\sqrt{N}} \sum_{\mathbf{k}} a_{\mathbf{k}m} \exp(-i\mathbf{k}\cdot(\mathbf{R}_n + \mathbf{r}_m)) \end{aligned} \tag{12}$$

$$\sum_{n,m} a_{n,m}^\dagger a_{n,m} = \frac{1}{N} \sum_{\mathbf{k},\mathbf{k}',m} a_{\mathbf{k}m}^\dagger a_{\mathbf{k}',m} \exp\left[i(\mathbf{k}-\mathbf{k}')\cdot(\mathbf{R}_n + \mathbf{r}_m)\right] = \sum_{\mathbf{k}m} a_{\mathbf{k}m}^\dagger a_{\mathbf{k}m}$$

$$\begin{aligned} \sum_{\langle nm,n'm'\rangle} a_{n,m}^\dagger a_{n',m'} &= \frac{1}{N} \sum_{\langle nm,n'm'\rangle} \sum_{\mathbf{k},\mathbf{k}'} a_{\mathbf{k}m}^\dagger a_{\mathbf{k}'m'} \exp\left[i\mathbf{k}\cdot(\mathbf{R}_n + \mathbf{r}_m) - i\mathbf{k}'\cdot(\mathbf{R}_{n'} + \mathbf{r}_{m'})\right] \\ &= \sum_{\mathbf{k},\langle m,m'\rangle} a_{\mathbf{k}m}^\dagger a_{\mathbf{k}m'} \exp\left[i\mathbf{k}\cdot\Delta\mathbf{r}_{\langle nm,n'm'\rangle}\right] \\ \sum_{\langle nm,n'm'\rangle} a_{n,m} a_{n',m'} &= \frac{1}{N} \sum_{\langle nm,n'm'\rangle} \sum_{\mathbf{k},\mathbf{k}'} a_{\mathbf{k}m} a_{\mathbf{k}'m'} \exp\left[-i\mathbf{k}\cdot(\mathbf{R}_n + \mathbf{r}_m) - i\mathbf{k}'\cdot(\mathbf{R}_{n'} + \mathbf{r}_{m'})\right] \\ &= \sum_{\mathbf{k},\langle m,m'\rangle} a_{\mathbf{k}m} a_{-\mathbf{k}m'} \exp\left[-i\mathbf{k}\cdot\Delta\mathbf{r}_{\langle nm,n'm'\rangle}\right] \\ \sum_{\langle nm,n'm'\rangle} a_{n,m}^\dagger a_{n',m'}^\dagger &= \sum_{\mathbf{k},\langle m,m'\rangle} a_{\mathbf{k}m}^\dagger a_{-\mathbf{k}m'}^\dagger \exp\left[i\mathbf{k}\cdot\Delta\mathbf{r}_{\langle nm,n'm'\rangle}\right] \end{aligned} \tag{13}$$

Here, $\langle nm, n'm'\rangle = \langle ij\rangle$ denotes the summation over nearest-neighbor bonds connecting sublattice sites m and m' located in the n-th and n'-th unit cells, respectively. The notation $\langle m, m'\rangle$ refers to the same set of sublattice pairs, with m assumed to belong to the reference (zeroth) unit cell. The vector $\Delta\mathbf{r}_{\langle nm,n'm'\rangle} \equiv \mathbf{R}_n + \mathbf{r}_m - \mathbf{R}_{n'} - \mathbf{r}_{m'}$ denotes the spatial displacement between the connected sublattices.

After performing the Fourier transformation, the quadratic Hamiltonian in Eq.11 takes the form [65]

$$\begin{aligned} \mathcal{H}_2 = \sum_{\mathbf{k}} \sum_{m,m'=1}^{4} \Big\{ & A_{\mathbf{k}}^{mm'} a_{\mathbf{k}m}^\dagger a_{\mathbf{k}m'} \\ & + \frac{1}{2}\left[B_{\mathbf{k}}^{mm'} a_{\mathbf{k}m}^\dagger a_{-\mathbf{k}m'}^\dagger + (B_{\mathbf{k}}^{m'm})^* a_{-\mathbf{k}m} a_{\mathbf{k}m'}\right]\Big\} \end{aligned} \tag{14}$$

The hermiticity of Eq.14 and the symmetry under relabeling $\mathbf{k} \to -\mathbf{k}$ imply that

$$A_{\mathbf{k}}^{mm'} = (A_{\mathbf{k}}^{m'm})^* \quad B_{\mathbf{k}}^{mm'} = B_{-\mathbf{k}}^{m'm} \tag{15}$$

S3.2 Multi-flavor Bogoliubov Transformations

The Hamiltonian in Eq.14 can be diagonalized by multi-flavor bogoliubov transformations [65, 66]. To proceed, we define the 4-component column vectors:

$$a_{\mathbf{k}} = \begin{pmatrix} a_{\mathbf{k}1} \\ a_{\mathbf{k}2} \\ a_{\mathbf{k}3} \\ a_{\mathbf{k}4} \end{pmatrix} \quad a_{\mathbf{k}}^* = \begin{pmatrix} a_{\mathbf{k}1}^\dagger \\ a_{\mathbf{k}2}^\dagger \\ a_{\mathbf{k}3}^\dagger \\ a_{\mathbf{k}4}^\dagger \end{pmatrix} \tag{16}$$

and the adjoint row vectors

$$\begin{aligned} a_{\mathbf{k}}^\dagger &= (a_{\mathbf{k}1}^\dagger, a_{\mathbf{k}2}^\dagger, a_{\mathbf{k}3}^\dagger, a_{\mathbf{k}4}^\dagger) \\ a_{\mathbf{k}}^T &= (a_{\mathbf{k}1}, a_{\mathbf{k}2}, a_{\mathbf{k}3}, a_{\mathbf{k}4}) \end{aligned} \tag{17}$$

These vectors can be combined to 8-components vectors,

$$\boldsymbol{\phi}_{\mathbf{k}} = \begin{pmatrix} a_{\mathbf{k}} \\ a_{-\mathbf{k}}^* \end{pmatrix} = \begin{pmatrix} a_{\mathbf{k}1} \\ a_{\mathbf{k}2} \\ a_{\mathbf{k}3} \\ a_{\mathbf{k}4} \\ a_{-\mathbf{k}1}^\dagger \\ a_{-\mathbf{k}2}^\dagger \\ a_{-\mathbf{k}3}^\dagger \\ a_{-\mathbf{k}4}^\dagger \end{pmatrix} \tag{18}$$

$$\begin{aligned} \boldsymbol{\phi}_{\mathbf{k}}^\dagger &= (a_{\mathbf{k}}^\dagger, a_{-\mathbf{k}}^T) \\ &= (a_{\mathbf{k}1}^\dagger, a_{\mathbf{k}2}^\dagger, a_{\mathbf{k}3}^\dagger, a_{\mathbf{k}4}^\dagger, a_{-\mathbf{k}1}, a_{-\mathbf{k}2}, a_{-\mathbf{k}3}, a_{-\mathbf{k}4}) \end{aligned} \tag{19}$$

Eq.14 can now be written in a compact form

$$\mathcal{H}_2 = \frac{1}{2}\sum_{\mathbf{k}} \left[\phi_{\mathbf{k}}^\dagger \mathbb{M}_{\mathbf{k}} \phi_{\mathbf{k}} - \mathrm{Tr}\mathbf{A}_{\mathbf{k}}\right] \tag{20}$$

where

$$\mathbb{M}_{\mathbf{k}} = \begin{pmatrix} \mathbf{A}_{\mathbf{k}} & \mathbf{B}_{\mathbf{k}} \\ \mathbf{B}_{\mathbf{k}}^\dagger & \mathbf{A}_{-\mathbf{k}}^T \end{pmatrix} = \begin{pmatrix} \mathbf{A}_{\mathbf{k}} & \mathbf{B}_{\mathbf{k}} \\ \mathbf{B}_{-\mathbf{k}}^* & \mathbf{A}_{-\mathbf{k}}^* \end{pmatrix}, \tag{21}$$

$[\mathbf{A}_{\mathbf{k}}]^{mm'} \equiv A_{\mathbf{k}}^{mm'}$ and $[\mathbf{B}_{\mathbf{k}}]^{mm'} \equiv B_{\mathbf{k}}^{mm'}$ are 4×4 block matrix satisfying $\mathbf{A}_{\mathbf{k}} = \mathbf{A}_{\mathbf{k}}^\dagger$ and $\mathbf{B}_{\mathbf{k}} = \mathbf{B}_{-\mathbf{k}}^T$.

To diagonalize Eq. 20, we introduce a new set of boson operators $b_{\mathbf{k}1}$, $b_{\mathbf{k}2}$, $b_{\mathbf{k}3}$, and $b_{\mathbf{k}4}$, and define the vector

$$\boldsymbol{\psi}_{\mathbf{k}} = \begin{pmatrix} b_{\mathbf{k}} \\ b_{-\mathbf{k}}^* \end{pmatrix} = \begin{pmatrix} b_{\mathbf{k}1} \\ b_{\mathbf{k}2} \\ b_{\mathbf{k}3} \\ b_{\mathbf{k}4} \\ b_{-\mathbf{k}1}^\dagger \\ b_{-\mathbf{k}2}^\dagger \\ b_{-\mathbf{k}3}^\dagger \\ b_{-\mathbf{k}4}^\dagger \end{pmatrix} \tag{22}$$

We apply the transformation

$$\boldsymbol{\phi}_{\mathbf{k}} = \mathbb{T}_{\mathbf{k}} \boldsymbol{\psi}_{\mathbf{k}} \tag{23}$$

to Eq. 20, yielding

$$\mathcal{H}_2 = \frac{1}{2}\sum_{\mathbf{k}} \left[\psi_{\mathbf{k}}^\dagger \mathbb{T}_{\mathbf{k}}^\dagger \mathbb{M}_{\mathbf{k}} \mathbb{T}_{\mathbf{k}} \psi_{\mathbf{k}} - \mathrm{Tr}\,\mathbf{A}_{\mathbf{k}}\right] \tag{24}$$

The transformation matrix $\mathbb{T}_{\mathbf{k}}$ is an 8×8 matrix that must satisfy the following conditions:

(1) Diagonalization: The Hamiltonian is diagonalized by $\mathbb{T}_{\mathbf{k}}$:

$$\mathbb{D}_{\mathbf{k}} = \mathbb{T}_{\mathbf{k}}^\dagger \mathbb{M}_{\mathbf{k}} \mathbb{T}_{\mathbf{k}} \tag{25}$$

where $\mathbb{D}_{\mathbf{k}}$ is diagonal with eigenvalues $d_{\mathbf{k}i}$.

(2) Bosonic Commutation Relations: The transformed operators must satisfy canonical boson commutation relations:

$$\mathbb{T}_{\mathbf{k}}^\dagger \mathbb{G} \mathbb{T}_{\mathbf{k}} = \mathbb{G} = \mathbb{T}_{\mathbf{k}} \mathbb{G} \mathbb{T}_{\mathbf{k}}^\dagger \tag{26}$$

with the metric matrix

$$\mathbb{G} = \begin{pmatrix} \mathbf{1}_{4\times 4} & 0 \\ 0 & -\mathbf{1}_{4\times 4} \end{pmatrix} \tag{27}$$

Thus, $\mathbb{T}_{\mathbf{k}}$ is a symplectic matrix, not unitary.

(3) Permutation Condition: Define the permutation matrix:

$$\mathbb{P} = \begin{pmatrix} 0 & \mathbf{1}_{4\times 4} \\ \mathbf{1}_{4\times 4} & 0 \end{pmatrix} \tag{28}$$

We require:

$$\boldsymbol{\phi}_{-\mathbf{k}}^* = \mathbb{P}\boldsymbol{\phi}_{\mathbf{k}} \tag{29}$$

$$\boldsymbol{\psi}_{-\mathbf{k}}^* = \mathbb{P}\boldsymbol{\psi}_{\mathbf{k}} \tag{30}$$

which implies:

$$\mathbb{P}\mathbb{T}_{\mathbf{k}} = \mathbb{T}_{-\mathbf{k}}^* \mathbb{P}, \quad \mathbb{P}\mathbb{T}_{\mathbf{k}}\mathbb{P} = \mathbb{T}_{-\mathbf{k}}^* \tag{31}$$

Hence, $\mathbb{T}_{-\mathbf{k}}$ can be derived from $\mathbb{T}_{\mathbf{k}}$, and has a block structure:

$$\mathbb{T}_{\mathbf{k}} = \begin{pmatrix} \mathbf{Q}_{\mathbf{k}} & \mathbf{R}_{\mathbf{k}} \\ \mathbf{R}_{-\mathbf{k}}^* & \mathbf{Q}_{-\mathbf{k}}^* \end{pmatrix} \tag{32}$$

with $\mathbf{Q}_{\mathbf{k}}$ and $\mathbf{R}_{\mathbf{k}}$ as independent 4×4 matrices.

To numerically obtain the Bogoliubov transformation, we define:

$$\mathbb{T}_{\mathbf{k}} = (\boldsymbol{v}_{\mathbf{k}1}, \boldsymbol{v}_{\mathbf{k}2}, \ldots, \boldsymbol{v}_{\mathbf{k}8}) \tag{33}$$

Conditions (1) and (2) become:

$$\boldsymbol{v}_{\mathbf{k}i}^\dagger \mathbb{M}_{\mathbf{k}} \boldsymbol{v}_{\mathbf{k}j} = \delta_{ij} d_{\mathbf{k}i} \tag{34}$$

$$\boldsymbol{v}_{\mathbf{k}i}^\dagger \mathbb{G} \boldsymbol{v}_{\mathbf{k}j} = g_{ij} \tag{35}$$

with $g_{ij} = \delta_{ij}$ for $i \le 4$ and $g_{ij} = -\delta_{ij}$ for $i > 4$.

This leads to the generalized eigenvalue problem:

$$\mathbb{M}_{\mathbf{k}} \boldsymbol{v}_{\mathbf{k}} = \omega \mathbb{G} \boldsymbol{v}_{\mathbf{k}} \tag{36}$$

which is equivalent to

$$\mathbb{M}_{\mathbf{k}}^{\mathrm{dyn}} \boldsymbol{v}_{\mathbf{k}} = \omega \boldsymbol{v}_{\mathbf{k}} \tag{37}$$

here we define $\mathbb{M}_{\mathbf{k}}^{\mathrm{dyn}}$ which is non-Hermitian. Suppose we find 8 linearly independent eigenvectors $\{\boldsymbol{v}_{\mathbf{k}i}\}$ satisfying Eq. 37 and normalize them to obey Eq. 35, then by construction we have

$$\boldsymbol{v}_{\mathbf{k}i}^\dagger \mathbb{M}_{\mathbf{k}} \boldsymbol{v}_{\mathbf{k}j} = \omega_{\mathbf{k}j} \boldsymbol{v}_{\mathbf{k}i}^\dagger \mathbb{G} \boldsymbol{v}_{\mathbf{k}j} = \delta_{ij} \omega_{\mathbf{k}i} g_{ii} \tag{38}$$

implying $d_{\mathbf{k}i} = \omega_{\mathbf{k}i} g_{ii}$. $\omega_{\mathbf{k}i}$ is therefore real and corresponds to $d_{\mathbf{k}i}$ up to a possible sign change.

From the Hermiticity of $\mathbb{M}_{\mathbf{k}}$, we find:

$$0 = (\mathbb{M}_{\mathbf{k}} \boldsymbol{v}_{\mathbf{k}i})^\dagger \boldsymbol{v}_{\mathbf{k}j} - \boldsymbol{v}_{\mathbf{k}i}^\dagger \mathbb{M}_{\mathbf{k}} \boldsymbol{v}_{\mathbf{k}j} = (\omega_{\mathbf{k}i} - \omega_{\mathbf{k}j}) \boldsymbol{v}_{\mathbf{k}i}^\dagger \mathbb{G} \boldsymbol{v}_{\mathbf{k}j} \tag{39}$$

where $\boldsymbol{v}_{\mathbf{k}i}$ and $\boldsymbol{v}_{\mathbf{k}j}$ are two linearly independent eigenvectors ($i \neq j$). This procedure ensures that the bosonic commutation condition [Eq. 35] is satisfied when $\omega_{\mathbf{k}i} \neq \omega_{\mathbf{k}j}$. In the case of degenerate eigenvalues, it is necessary to apply a generalized Gram-Schmidt orthogonalization:

$$\boldsymbol{v}_{\mathbf{k}i} \to \boldsymbol{v}_{\mathbf{k}i} - \sum_{j=i+1}^{m} \boldsymbol{v}_{\mathbf{k}j} \frac{\boldsymbol{v}_{\mathbf{k}i}^\dagger \mathbb{G} \boldsymbol{v}_{\mathbf{k}j}}{\boldsymbol{v}_{\mathbf{k}j}^\dagger \mathbb{G} \boldsymbol{v}_{\mathbf{k}j}}, \quad i = 1, \ldots, m-1, \tag{40}$$

to enforce the generalized orthogonality condition $\boldsymbol{v}_{\mathbf{k}i}^\dagger \mathbb{G} \boldsymbol{v}_{\mathbf{k}j} = 0$ for vectors $i \neq j$ corresponding to degenerate values of $\omega_{\mathbf{k}}$.

In practice, we begin by diagonalizing the dynamical matrix $\mathbb{M}_{\mathbf{k}}^{\mathrm{dyn}}$:

$$\tilde{\mathbb{T}}_{\mathbf{k}} = (\tilde{\boldsymbol{v}}_{\mathbf{k}1}, \tilde{\boldsymbol{v}}_{\mathbf{k}2}, \ldots, \tilde{\boldsymbol{v}}_{\mathbf{k}8}), \tag{41}$$

$$\tilde{\mathbb{D}}_{\mathbf{k}} = \tilde{\mathbb{T}}_{\mathbf{k}}^{-1} \mathbb{M}_{\mathbf{k}}^{\mathrm{dyn}} \tilde{\mathbb{T}}_{\mathbf{k}}. \tag{42}$$

We then normalize and orthogonalize the eigenvectors $\{\tilde{\boldsymbol{v}}_{\mathbf{k}i}\}$ in two steps. First, we normalize each vector as:

$$\tilde{\boldsymbol{v}}_{\mathbf{k}i} \to \frac{\tilde{\boldsymbol{v}}_{\mathbf{k}i}}{\left(\tilde{\boldsymbol{v}}_{\mathbf{k}i}^{\dagger} \mathbb{G} \tilde{\boldsymbol{v}}_{\mathbf{k}i}\right)}, \quad i = 1, \ldots, 8. \tag{43}$$

Next, for each degenerate subspace of dimension m, consisting of eigenvectors $\{\tilde{\boldsymbol{v}}_{\mathbf{k}n}, \tilde{\boldsymbol{v}}_{\mathbf{k}n+1}, \ldots, \tilde{\boldsymbol{v}}_{\mathbf{k}n+m}\}$, we apply a generalized Gram-Schmidt orthogonalization:

$$\tilde{\boldsymbol{v}}_{\mathbf{k}i} \to \tilde{\boldsymbol{v}}_{\mathbf{k}i} - \sum_{j=i+1}^{n+m} \tilde{\boldsymbol{v}}_{\mathbf{k}j} \frac{\tilde{\boldsymbol{v}}_{\mathbf{k}i}^{\dagger} \mathbb{G} \tilde{\boldsymbol{v}}_{\mathbf{k}j}}{\tilde{\boldsymbol{v}}_{\mathbf{k}j}^{\dagger} \mathbb{G} \tilde{\boldsymbol{v}}_{\mathbf{k}j}}, \quad i = n, \ldots, n+m-1. \tag{44}$$

This iterative process yields a normalized and orthogonal set of eigenvectors $\{\boldsymbol{v}_{\mathbf{k}i}\}$ that satisfy Eqs. 34 and 35, thereby enabling the construction of $\mathbb{T}_{\mathbf{k}}$ and $\mathbb{T}_{-\mathbf{k}}$ using Eqs. 33 and 31. Substituting Eq.23 to Eq.24 gives

$$\mathcal{H}_2 = \sum_{\mathbf{k}} \sum_{\lambda=1}^{4} \omega_{\mathbf{k}\lambda} \left(b_{\mathbf{k}\lambda}^{\dagger} b_{\mathbf{k}\lambda} + \frac{1}{2} \right) \tag{45}$$

The four bands of magnon consist of two degenerate flat modes and two dispersive modes.

S3.3 Calculation of Magnetic Structure Factor

The structure factor for magnetic neutron scattering is

$$\begin{aligned} \mathcal{S}(\mathbf{k}, \omega) = & \int_{-\infty}^{\infty} dt \exp(-i\omega t) \sum_{\mu\nu} (\delta_{\mu\nu} - \frac{k_\mu k_\nu}{k^2}) \\ & \times \langle m^{\mu}(-\mathbf{k}, 0) m^{\nu}(\mathbf{k}, t) \rangle \end{aligned} \tag{46}$$

Here μ, ν labels the global $\hat{x}$, $\hat{y}$, $\hat{z}$ directions. We focus on the correlation function:

$$\begin{aligned} & \langle m^{\mu}(-\mathbf{k}, 0) m^{\nu}(\mathbf{k}, t) \rangle \\ = & \sum_{\alpha,\beta=1}^{4} \langle m_{\alpha}(-\mathbf{k}, 0) m_{\beta}(\mathbf{k}, t) (\hat{z}_{\alpha} \cdot \hat{\mu}) (\hat{z}_{\beta} \cdot \hat{\nu}) \rangle \end{aligned} \tag{47}$$

Here, m_α and m_β are the magnetic moments on sublattices α and β, respectively. Following Eqs. 78, we have the real-space expression

$$m_{n,\alpha} = g_z \mu_{\mathrm{B}} (\cos(\vartheta) \tilde{\tau}_{n,\alpha}^{\tilde{z}} + \sin(\vartheta) \tilde{\tau}_{n,\alpha}^{\tilde{x}}) \tag{48}$$

where n labels the unit cell. We note that correlation functions between the $\tilde{\tau}^{\tilde{z}}$ components give rise to static long-range correlations, which result in magnetic Bragg peaks associated with the AIAO phase. In contrast, correlations between the $\tilde{\tau}^{\tilde{x}}$ components generate dynamical spin-wave excitations. Focus on the spin-wave excitation, we have (omitting the time label for now)

$$\begin{aligned} m_{\beta}^{\tilde{x}}(\mathbf{k}) = & \frac{1}{\sqrt{N}} \sum_{n} \exp(-i\mathbf{k} \cdot (\mathbf{R}_{\mathbf{n}} + \mathbf{r}_{\beta})) \\ & \times \frac{\sqrt{2S}}{2} (a_{n,\beta} + a_{n,\beta}^{\dagger}) \cdot (g_{zz} \mu_{\mathrm{B}} \sin(\vartheta)) \end{aligned} \tag{49}$$

Substitute the definition in Eq.12 into the above equations gives

$$m_{\beta}^{\tilde{x}}(\mathbf{k}) = \frac{\sqrt{2S}}{2} g_{zz} \mu_{\mathrm{B}} \sin(\vartheta) (a_{\mathbf{k}\beta}^{\dagger} + a_{-\mathbf{k}\beta}) \tag{50}$$

and similiarly,

$$m_{\alpha}^{\tilde{x}}(-\mathbf{k}) = \frac{\sqrt{2S}}{2} g_{zz} \mu_{\mathrm{B}} \sin(\vartheta) (a_{-\mathbf{k}\alpha}^{\dagger} + a_{\mathbf{k}\alpha}) \tag{51}$$

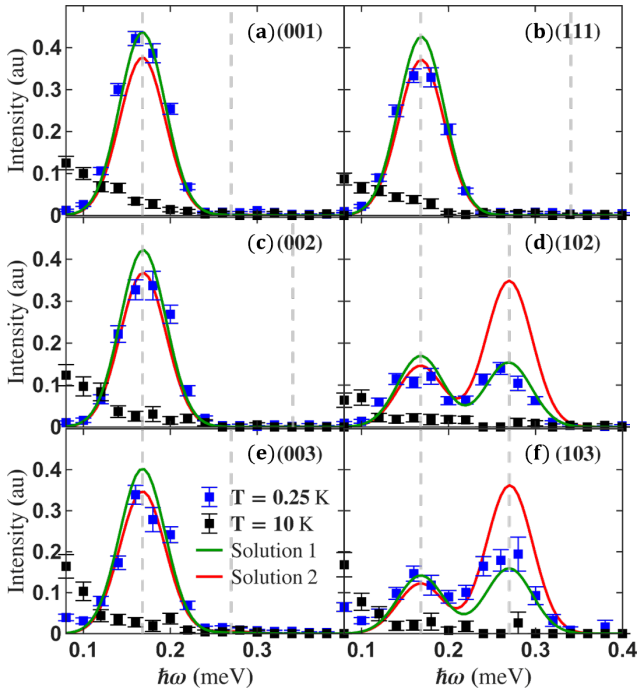

FIG. S6. Additional data. (a–f) Constant-Q energy cuts at the indicated positions, integrated over $[-0.1, 0.1]$ rlu along each principal reciprocal-space direction and measured with $E_i = 2.19$ meV. Blue/black curves: $T = 0.25$ K/10 K. Green/red curves: simulations for Solution 1 (Eq. 68)/Solution 2 (Eq. 69), averaged over the same Q-windows as the data and convolved with the LET instrumental energy resolution at $E_i = 2.19$ meV and scaled by the same independent global factors used in Fig. 3 of the main text, so that the combined simulated intensity across (a–f) and Fig. 3(a–d) matches experiment. Data in (a,b,c,e) are averaged over symmetry-equivalent $\mathbf{Q}$ points in the (HHL) plane using the $Fd\bar{3}m$ space-group symmetry; (d,f) are not symmetrized. Gray dashed lines mark the calculated spin-wave energies.

With the definition in Eq.18, we have

$$\begin{aligned}&\langle m_\alpha^{\tilde{x}}(-\mathbf{k},0)m_\beta^{\tilde{x}}(\mathbf{k},t)\rangle\\ =&\frac{S}{2}(g_z\mu_{\mathrm{B}}\sin(\vartheta))^2\Big\langle(\boldsymbol{\phi}_{\mathbf{k}\alpha}(0)+\boldsymbol{\phi}_{\mathbf{k}\alpha+4}(0))\\ &\times(\boldsymbol{\phi}_{-\mathbf{k}\beta}(t)+\boldsymbol{\phi}_{-\mathbf{k}\beta+4}(t))\Big\rangle\end{aligned}\tag{52}$$

Substitution the Bogoliubov transformation in Eq.22.23

$$\begin{aligned}&\langle m_\alpha^{\tilde{x}}(-\mathbf{k},0)m_\beta^{\tilde{x}}(\mathbf{k},t)\rangle\\ =&\frac{S}{2}(g_z\mu_{\mathrm{B}}\sin(\vartheta))^2\\ &\times\Big\langle\sum_\lambda\left(\mathbb{T}_{\mathbf{k}}^{\alpha,\lambda}\boldsymbol{\psi}_{\mathbf{k}\lambda}(0)+\mathbb{T}_{\mathbf{k}}^{\alpha+4,\lambda}\boldsymbol{\psi}_{\mathbf{k}\lambda}(0)\right)\\ &\times\sum_{\lambda'}\left(\mathbb{T}_{-\mathbf{k}}^{\beta,\lambda'}\boldsymbol{\psi}_{-\mathbf{k}\lambda'}(t)+\mathbb{T}_{-\mathbf{k}}^{\beta+4,\lambda'}\boldsymbol{\psi}_{-\mathbf{k}\lambda'}(t)\right)\Big\rangle\end{aligned}\tag{53}$$

The results of Eq.53 consist of a polynomial of $\langle b_\lambda^{(\dagger)}b_{\lambda'}^{(\dagger)}\rangle$. For low temperature below the gap energy Δ_1 of the flat modes ($k_{\mathrm{B}}T\ll\Delta_1$), we only need to consider the ground state (vaccum of b_λ) in the thermal average $\langle ...\rangle$, and keep the terms as

$$\begin{aligned}\int_{-\infty}^{\infty}dt\,e^{-i\omega t}\langle b_{\mathrm{k}\lambda}b_{\mathrm{k}\lambda}^\dagger\rangle&=(1+n_{\mathrm{B}}(\omega))\,\delta(\omega-\omega_{\mathbf{k}\lambda})\\ \int_{-\infty}^{\infty}dt\,e^{-i\omega t}\langle b_{\mathrm{k}\lambda}^\dagger b_{\mathrm{k}\lambda}\rangle&=n_{\mathrm{B}}(-\omega)\,\delta(\omega+\omega_{\mathbf{k}\lambda})\end{aligned}\tag{54}$$

where $n_{\mathrm{B}}(\omega)=1/(\exp(\hbar\omega/k_{\mathrm{B}}T)-1)$ is the bosonic distribution function.

The neutron cross section on the energy-loss side ($\hbar\omega>0$) is then

$$\begin{aligned}&\langle m_\alpha^{\tilde{x}}(-\mathbf{k},0)m_\beta^{\tilde{x}}(\mathbf{k},t)\rangle\\ =&\frac{S}{2}(g_z\mu_{\mathrm{B}}\sin(\vartheta))^2\\ &\times\sum_\lambda(\mathbb{T}_{\mathbf{k}}^{\alpha,\lambda}\mathbb{T}_{-\mathbf{k}}^{\beta,\lambda+4}+\mathbb{T}_{\mathbf{k}}^{\alpha,\lambda}\mathbb{T}_{-\mathbf{k}}^{\beta+4,\lambda+4}\\ &+\mathbb{T}_{\mathbf{k}}^{\alpha+4,\lambda}\mathbb{T}_{-\mathbf{k}}^{\beta,\lambda+4}+\mathbb{T}_{\mathbf{k}}^{\alpha+4,\lambda}\mathbb{T}_{-\mathbf{k}}^{\beta+4,\lambda+4})\langle b_{\mathbf{k}\lambda}b_{\mathbf{k}\lambda}^\dagger\rangle\end{aligned}\tag{55}$$

Similarly, we could the derive cross section on the energy-gain side ($\hbar\omega<0$) by the detailed-balance equation $S(-\mathbf{k},-\omega)=\exp(-\hbar\omega/k_{\mathrm{B}}T)S(\mathbf{k},\omega)$. Substituting these into Eq. 46 yields the dynamical magnetic neutron structure factor:

$$\begin{aligned}\mathcal{S}^{\tilde{x}}(\mathbf{k},\omega)=\frac{S}{2}(g_z\mu_{\mathrm{B}}\sin\vartheta)^2\sum_{\mu,\nu}\left(\delta_{\mu\nu}-\frac{k_\mu k_\nu}{k^2}\right)\\ \times\sum_{\lambda=1}^{4}s_\lambda(\mathbf{k})\left[(1+n_{\mathrm{B}}(\omega))\,\delta(\omega-\omega_{\mathbf{k}\lambda})\right.\\ \left.+n_{\mathrm{B}}(-\omega)\,\delta(\omega+\omega_{\mathbf{k}\lambda})\right]\end{aligned}\tag{56}$$

where we define the coefficients for the four modes as

$$\begin{aligned}s_\lambda(\mathbf{k})=&\sum_{\alpha,\beta=1}^{4}(\hat{z}_\alpha\cdot\hat{\mu})(\hat{z}_\beta\cdot\hat{\nu})\\ &\times(\mathbb{T}_{\mathbf{k}}^{\alpha,\lambda}\mathbb{T}_{-\mathbf{k}}^{\beta,\lambda+4}+\mathbb{T}_{\mathbf{k}}^{\alpha,\lambda}\mathbb{T}_{-\mathbf{k}}^{\beta+4,\lambda+4}\\ &+\mathbb{T}_{\mathbf{k}}^{\alpha+4,\lambda}\mathbb{T}_{-\mathbf{k}}^{\beta,\lambda+4}+\mathbb{T}_{\mathbf{k}}^{\alpha+4,\lambda}\mathbb{T}_{-\mathbf{k}}^{\beta+4,\lambda+4})\end{aligned}\tag{57}$$

For comparison with the experimentally measured neutron scattering cross section,

$$\frac{d^2\sigma}{d\Omega\,dE_f}(\mathbf{k},\omega)=\frac{k_f}{k_i}(\gamma r_0)^2|f(\mathbf{k})|^2\mathcal{S}^{\tilde{x}}(\mathbf{k},\omega),\tag{58}$$

we multiply the calculated dynamical magnetic structure factor $\mathcal{S}^{\tilde{x}}(\mathbf{k},\omega)$ by the squared magnetic form factor $|f(\mathbf{k})|^2$ of Nd^{3+} ions. In Eq. 58, $r_0=2.818\times10^{-15}$ m is the classical electron radius, and $\gamma=-1.913$ is the magnetic dipole moment of the neutron in units of the nuclear Bohr magneton. The quantities k_i and k_f denote the incident and scattered neutron momenta, respectively. These prefactors do not affect the $\mathbf{k}$-dependence of the observed inelastic signal.

S3.4 Evaluation of Rotation Angle ϑ

To estimate the fraction of ordered moment in the ground state relative to the total moment of Nd^{3+} in this model, we calculate [25]

$$\langle\tilde{\tau}_i^{\tilde{z}}\rangle=S-\langle a_{n,m}^\dagger a_{n,m}\rangle,\tag{59}$$

where site i is again specified by the unit cell n and one of the four sublattices m. Using Eqs. 13, 18, and 23, we obtain

$$\begin{aligned}\langle a_{n,m}^\dagger a_{n,m}\rangle&=\frac{1}{N}\sum_{\mathbf{k}}\langle a_{\mathbf{k}m}^\dagger a_{\mathbf{k}m}\rangle\\ &=\frac{1}{N}\sum_{\mathbf{k}}\langle\boldsymbol{\phi}_{-\mathbf{k},m+4}\,\boldsymbol{\phi}_{\mathbf{k},m}\rangle\\ &=\frac{1}{N}\sum_{\mathbf{k}}\sum_{\lambda,\lambda'=1}^{4}\langle\mathbb{T}_{-\mathbf{k}}^{m+4,\lambda}\,\boldsymbol{\psi}_{-\mathbf{k},\lambda}\,\mathbb{T}_{\mathbf{k}}^{m,\lambda'}\,\boldsymbol{\psi}_{\mathbf{k},\lambda'}\rangle.\end{aligned}\tag{60}$$

At zero temperature, only the bilinear term $\langle b_{\mathbf{k}\lambda}b_{\mathbf{k}\lambda}^\dagger\rangle=1$ contributes, yielding

$$\langle a_{n,m}^\dagger a_{n,m}\rangle=\frac{1}{N}\sum_{\mathbf{k}}\sum_{\lambda=1}^{4}\mathbb{T}_{-\mathbf{k}}^{m+4,\lambda}\,\mathbb{T}_{\mathbf{k}}^{m,\lambda+4}.\tag{61}$$

In practice, we use a $10\times10\times10$ array of conventional cubic unit cells (along $\hat{x}$, $\hat{y}$, and $\hat{z}$), sum over 4,000 $\mathbf{k}$ points in the first Brillouin zone, and set $N=4{,}000$ in Eq. (61). The fraction of ordered moment is then given by

$$\frac{m_{\mathrm{ord}}}{m_{\mathrm{sat}}}=\cos\vartheta\left(\frac{S-\langle a_{n,m}^\dagger a_{n,m}\rangle}{S}\right).\tag{62}$$

S3.5 Calculation of Heat Capacity from Spin-wave Excitations

Using the interaction parameters and linear spin-wave spectra obtained in Sec. S4, we numerically evaluate the single-particle density of states $g(E)$ (normalized per Nd ion such that $\int_0^\infty g(E)\,dE = 1$) and compute the spin-wave contribution to the specific heat $C_{\rm SW}$ following the standard bosonic formalism [67]:

$$\begin{aligned} C_{\rm SW}(T) &= \int_0^\infty dE\, g(E)\, c(E,T), \\ c(E,T) &= k_{\rm B}\left(\frac{E}{k_{\rm B}T}\right)^2 \frac{\exp(E/k_{\rm B}T)}{\left[\exp(E/k_{\rm B}T)-1\right]^2}. \end{aligned} \tag{63}$$

The resulting $C_{\rm SW}(T)$ curve , converted to the same unit as the measurement, is presented in Fig. 1(b) of the main text. For low temperature $k_{\rm B}T \ll \Delta_1$ [Eq.64], $C_{\rm SW}$ is dominated by the flat band excitations at $E = \Delta_1$ and we approximately have $C_{\rm SW} \propto (1/T^2)\exp(-\Delta_1/k_{\rm B}T)$ [28].

S4. DETERMINATION OF INTERACTION PARAMETERS

Following Ref. [28], we extract the interaction parameters $\tilde{J}_x$, $\tilde{J}_y$, and $\tilde{J}_z$ from the analytical expressions of the spin-wave energies at the zone center (000) and the zone boundary (100). The two degenerate flat modes occur at the energy transfer

$$\Delta_1 = \sqrt{(3|\tilde{J}_z| - \tilde{J}_x)(3|\tilde{J}_z| - \tilde{J}_y)}. \tag{64}$$

At the zone boundary (100), the dispersive modes reach the energy Δ_2, while at the zone center (000) the higher-energy dispersive mode appears at Δ_3:

$$\Delta_2 = \sqrt{(3|\tilde{J}_z| + \tilde{J}_x)(3|\tilde{J}_z| + \tilde{J}_y)}, \tag{65}$$

$$\Delta_3 = 3\sqrt{(|\tilde{J}_z| + \tilde{J}_x)(|\tilde{J}_z| + \tilde{J}_y)}. \tag{66}$$

By fitting energy cut taken at high symmetry points as presented in Fig. 3 (in main text) and Fig. S6, we obtain

$$\begin{aligned} \Delta_1 &= 0.168(2)\ \text{meV} \\ \Delta_2 &= 0.270(4)\ \text{meV} \\ \Delta_3 &= 0.341(5)\ \text{meV} \end{aligned} \tag{67}$$

By solving the Eqs.64,65,66, we obtain two set of solutions,

$$\begin{aligned} \tilde{J}_x &= 0.1002^{+0.0133}_{-0.0164}\ \text{meV} \\ \tilde{J}_y &= -0.0012^{+0.0116}_{-0.0086}\ \text{meV} \\ \tilde{J}_z &= -0.0750^{+0.0017}_{-0.0016}\ \text{meV} \end{aligned} \tag{68}$$

and

$$\begin{aligned} \tilde{J}_x &= -0.0012^{+0.0116}_{-0.0086}\ \text{meV} \\ \tilde{J}_y &= 0.1002^{+0.0133}_{-0.0164}\ \text{meV} \\ \tilde{J}_z &= -0.0750^{+0.0017}_{-0.0016}\ \text{meV} \end{aligned} \tag{69}$$

The simulated spin-wave structure factors based on the parameters in Eq. 68 and Eq. 69 are shown in Fig. 3 and Fig. S6 alongside the experimental data. After convolution with the instrumental energy resolution, the simulated linewidths exhibit excellent agreement with the measurements. Each simulated curve is rescaled by an independent overall factor (per solution) to match the total experimental intensity. Among the two models, Solution 1 (Eq. 68) provides a noticeably better description of the data, particularly in reproducing the relative intensity of the lower flat modes and the higher dispersive modes. We therefore identify Solution 1 (Eq. 68) as the correct set of parameters for the $Nd_2Sn_2O_7$ system.

Using Eq. 60, we numerically evaluate the reduction of the ordered moment due to zero-point quantum fluctuations in the ground state [25, 28]:

$$\begin{aligned} \langle a^\dagger_{n,m} a_{n,m}\rangle &= 0.0171^{+0.0122}_{-0.0085}, \\ \frac{S - \langle a^\dagger_{n,m} a_{n,m}\rangle}{S} &= 0.9658^{+0.0169}_{-0.0244}. \end{aligned} \tag{70}$$

Using Eq. 62, $m_{\rm ord} = 1.708(3)\ \mu_{\rm B}/{\rm Nd}^{3+}$ [35], and $m_{\rm sat} = 2.387(5)\ \mu_{\rm B}/{\rm Nd}^{3+}$ from our Curie-Weiss fit (see Sec. S5), we obtain the rotation-angle parameter ϑ defined in Eq. 5:

$$\vartheta = 42.5^{+1.1}_{-1.8}\ ^\circ = 0.741^{+0.019}_{-0.029}\ \text{radian}. \tag{71}$$

Taking together Eqs.68,71, we can inversely evaluate exchange parameters in the original local frame:

$$\begin{aligned} J_x &= \tilde{J}_x \cos^2\vartheta + \tilde{J}_z \sin^2\vartheta \\ J_y &= \tilde{J}_y \\ J_z &= \tilde{J}_z \cos^2\vartheta + \tilde{J}_x \sin^2\vartheta \\ J_{xz} &= (\tilde{J}_x - \tilde{J}_z)\sin\vartheta\cos\vartheta \end{aligned} \tag{72}$$

which yields

$$\begin{aligned} J_x &= 0.0204^{+0.0134}_{-0.0128}\ \text{meV} \\ J_y &= -0.0012^{+0.0116}_{-0.0086}\ \text{meV} \\ J_z &= 0.0048^{+0.0106}_{-0.0130}\ \text{meV} \\ J_{xz} &= 0.0873^{+0.0077}_{-0.0095}\ \text{meV} \end{aligned} \tag{73}$$

S5. DETAILS OF CURIE-WEISS FIT

When applying Curie–Weiss (CW) fits to the dc susceptibility with different temperature ranges, we observe variations in the extracted effective magnetic moment

$\mu_{\rm eff}$ and Curie–Weiss temperature $\theta_{\rm CW}$. To obtain the effective moment of the ground-state doublet, we restrict the fitting to temperatures well below the first excited crystal-field (CEF) level of Nd^{3+} in $Nd_2Sn_2O_7$, located at ∼26 meV [35, 55]. Table SII summarizes the fitting results for different temperature ranges. The fitted $\mu_{\rm eff}$ is largely consistent below 50 K, but gradually increases as the upper bound of the fit window is extended, reflecting the influence of higher CEF levels. By contrast, $\theta_{\rm CW}$ decreases systematically with increasing fit range.

For quantitative analysis, we adopt the low-temperature interval $[2, 10]$ K to evaluate the effective moment used in the ordered-to-saturated moment ratio [Eq. 62]. The value of the effective moment $\mu_{\rm eff}$ extracted from the Curie–Weiss fit is then used for the saturated moment $m_{\rm sat}$. For a system in which each magnetic ion hosts a ground-state doublet with strong Ising anisotropy, characterized by a dominant $g_\parallel$ and negligible transverse components $g_\perp \approx 0$, the powder-averaged effective moment is given by

$$\mu_{\rm eff}^2 = S(S+1)\,\frac{2g_\perp^2 + g_\parallel^2}{3}\,\mu_B^2 = \frac{1}{4}g_\parallel^2\mu_B^2 = m_{\rm sat}^2, \quad (74)$$

with $S = \frac{1}{2}$ [54]. We therefore take $m_{\rm sat} \approx \mu_{\rm eff} = 2.397(2)\,\mu_{\rm B}/Nd^{3+}$, in good agreement with the reported $m_{\rm sat}$ values for $Nd_2Zr_2O_7$ [21, 22] and $Nd_2Hf_2O_7$ [33].

The resulting rotation angle ϑ [Eq. 71] allows us to compute the CW temperature predicted by the model [25, 28]:

$$\begin{aligned}\theta_{\rm CW}^{\rm cal} &= \frac{1}{2k_{\rm B}}\left(\tilde{J}_z\cos^2\vartheta + \tilde{J}_x\sin^2\vartheta\right)\\ &= 0.028^{+0.056}_{-0.070}\ \text{K}\end{aligned} \quad (75)$$

which is roughly consistent with the fitted value $\theta_{\rm CW} = -0.08(1)$ K and with the trend that $\theta_{\rm CW}$ approaches zero when the fit is restricted to low temperature. The fitted results are also in agreement with powder measurements reported in Ref. [35] for the ranges $[5, 15]$ K and $[150, 300]$ K, the latter yielding $\mu_{\rm eff} = 3.399(2)\ \mu_{\rm B}$, close to the free-ion value of 3.62 $\mu_{\rm B}$ for Nd^{3+}.

TABLE SII. Curie–Weiss fitting results for the dc susceptibility over different temperature ranges. Listed are the effective magnetic moment $\mu_{\rm eff}$ and the Curie–Weiss temperature $\theta_{\rm CW}$.

Fit Range (K)	$\mu_{\rm eff}$ ($\mu_{\rm B}$)	$\theta_{\rm CW}$ (K)
2–10	2.397(2)	−0.08(1)
2–15	2.408(2)	−0.13(2)
2–20	2.425(3)	−0.23(3)
2–30	2.469(5)	−0.60(7)
2–40	2.514(6)	−1.1(1)
2–50	2.560(7)	−1.7(2)
5–15	2.415(3)	−0.20(3)
150–300	3.399(2)	−61.37(32)